

HYPER-REDUCTION FOR PARAMETRIZED TRANSPORT DOMINATED PROBLEMS VIA ONLINE-ADAPTIVE REDUCED MESHES*

NEERAJ SARNA[†] AND SARA GRUNDEL[‡]

Abstract. We propose an efficient residual minimization technique for the nonlinear model-order reduction of parameterized hyperbolic partial differential equations. Our nonlinear approximation space is a span of snapshots evaluated on a shifted spatial domain, and we compute our reduced approximation via residual minimization. To speed-up the residual minimization, we compute and minimize the residual on a (preferably small) subset of the mesh, the so-called reduced mesh. Due to the nonlinearity of our approximation space we show that, similar to the solution, the residual also exhibits transport-type behaviour. To account for this behaviour, we introduce online-adaptivity in the reduced mesh by "moving" it along the spatial domain with parameter dependent shifts. We also present an extension of our method to spatial transforms different from shifting. Numerical experiments showcase the effectiveness of our method and the inaccuracies resulting from a non-adaptive reduced mesh.

1 Introduction For some solution $u(x, z) \in \mathbb{R}$, consider a parametrized partial differential equation (PDE) given as

$$(1.1) \quad \partial_t u(x, z) + \mathcal{L}(u(x, z), z) = 0, \quad \forall (x, t, z) \in \Omega \times D \times \mathcal{Z}.$$

Here, $x \in \Omega \subset \mathbb{R}^d$ is a point in the space domain Ω , $\mathcal{Z} \subset \mathbb{R}^{p+1}$ is some parameter domain, $t \in D$ is a point in the time-domain and \mathcal{L} is some spatial differential operator. For some finite time $T > 0$, we include the time-domain $D := [0, T]$ in the parameter domain \mathcal{Z} and express \mathcal{Z} as $\mathcal{Z} = D \times \mathcal{P}$, where $\mathcal{P} \subset \mathbb{R}^p$ is some additional parameter domain. The solution's dependency on $\mu \in \mathcal{P}$ can encode, for instance, the change in the material properties, variation in length scales, changes in the background temperature, etc. The later sections of our article further elaborate on the relevance of \mathcal{P} , we refer to [22] for additional examples.

An exact solution to the above equation is often unavailable and one seeks a numerical approximation

$$u(\cdot, z) \approx u_N(\cdot, z) \in \mathcal{X}_N,$$

with \mathcal{X}_N being a N -dimensional finite-volume/element/difference-type space. We refer to u_N as the full-order model (FOM). In a multi-query setting where solutions at several different parameter instances are needed, due to the high-dimensionality of \mathcal{X}_N , computing a FOM is unaffordable. This motivates one to consider a reduced-order model (ROM).

A ROM splits the solution algorithm into an offline and an online phase and performs most of the expensive computations offline, thus making the online phase efficient. For some finite number of training parameters $\{z^{(i)}\}_{i=1, \dots, m} \subset \mathcal{Z}$, the offline phase computes the set of solution snapshots $\{u_N(\cdot, z^{(i)})\}_i$ that are used by the online phase to efficiently approximate the FOM. If the number of snapshots required to

*Submitted to the editors xxx

Funding: N.S and S.G are supported by the German Federal Ministry for Economic Affairs and Energy (BMWi) in the joint project "MathEnergy - Mathematical Key Technologies for Evolving Energy Grids", sub-project: Model Order Reduction (Grant number: 0324019B).

[†]Corresponding author, Max Planck Institute for Dynamics of Complex Technical Systems, Sandtorstr 1, 39106, Magdeburg, Germany, sarna@mpi-magdeburg.mpg.de

[‡]Max Planck Institute for Dynamics of Complex Technical Systems, Sandtorstr 1, 39106, Magdeburg, Germany, grundel@mpi-magdeburg.mpg.de

reasonably approximate the FOM are sufficiently small, then one can expect a ROM to be more efficient than the FOM. We refer to the review article [4] and the later sections of our article for further details of the offline and the online phase.

This work focuses on parametrized hyperbolic PDEs. For such equations, there is ample numerical and analytical evidence indicating that a ROM based on a linear approximation space is inefficient/inaccurate—a large number of solution snapshots are required to reasonably approximate the FOM. The inefficiency arises from the poor approximability of the solution set $\{u(\cdot, z) : z \in \mathcal{Z}\}$ (or the so-called solution manifold) in a linear space—we refer to [5, 6, 10, 18, 20, 31, 33] for proofs related to the slow m -width decay of these solution sets and the related numerical experiments. Poor accuracy of a linear approximation motivates us to consider a nonlinear approximation space. We consider a nonlinear approximation space based upon transformed snapshots, an introduction to which is as follows.

1.1 The transformed snapshot approach We introduce a spatial transform $\varphi(\cdot, z, z^{(i)}) : \Omega \rightarrow \Omega$, and approximate the solution $u_N(\cdot, z)$ in the space

$$(1.2) \quad \mathcal{X}_m(z) := \Pi(\text{span}\{u_N(\varphi(\cdot, z, z^{(i)}), z^{(i)})\}_{i \in \Lambda(z)}).$$

Assuming that $\mathcal{X}_N \subset L^2(\Omega)$, Π is a projection operator from $L^2(\Omega)$ to \mathcal{X}_N and will be useful later when we operate a discretization of the operator \mathcal{L} on functions in $\mathcal{X}_m(z)$. The set $\Lambda(z) \subseteq \{1, \dots, m\}$ is some z -dependent index set that selects solution snapshots used to approximate $u_N(\cdot, z)$. A preferred choice for $\Lambda(z)$ is the index of parameter samples that lie in some neighbourhood of the target parameter z [1, 18].

For a detailed discussion on the role of φ , we refer to [33, 34], here, we summarize the basic idea. Usually, the exact solution is discontinuous along the parameter domain i.e., the function $u(x, \cdot)$ is discontinuous. This prohibits its accurate approximation in a low-dimensional linear space. Therefore, for all $z \in \mathcal{Z}$, we introduce a $\varphi(x, z, \hat{z})$ such that the *transformed solution* $u(\varphi(x, z, \cdot), \cdot)$ is (at least) not discontinuous and sufficiently regular. This allows for a low-dimensional linear reduced approximation of the transformed solution. Indeed, $\mathcal{X}_m(z)$ is a standard linear reduced-basis approximation space for the transformed solution set $\{u(\varphi(\cdot, z, \hat{z}), \hat{z}) : \hat{z} \in \mathcal{Z}\}$ with the snapshots collected at $\hat{z} \in \{z^{(i)}\}_i$. For further clarity on the role of φ , we refer to the example in [Appendix A](#). Note that whether such a φ always exists for a general hyperbolic PDE is unclear, as yet. In the following, we will make due with an ansatz for φ that is accurate for the numerical experiments considered later.

1.1.1 The online and the offline phase We focus on devising an efficient algorithm to approximate the FOM in $\mathcal{X}_m(z)$. Following is a generic description of the online and the offline phases that we consider.

1. *Offline phase:* compute the solution snapshots $\{u_N(\cdot, z^{(i)})\}_i$ and the snapshots of the spatial transform $\{\varphi(\cdot, z^{(j)}, z^{(i)})\}_{i,j}$.
2. *Online phase:* perform two steps (a) using the snapshots $\{\varphi(\cdot, z^{(j)}, z^{(i)})\}_{i,j}$, approximate $\varphi(\cdot, z, z^{(i)})$ by $\varphi_m(\cdot, z, z^{(i)})$, and (b) approximate $u_N(\cdot, z)$ by

$$(1.3) \quad u_N(\cdot, z) \approx u_m(\cdot, z) \in \mathcal{X}_m(z),$$

where, without a change in notation, in $\mathcal{X}_m(z)$, φ is replaced by φ_m . Note that as compared to a linear ROM (see [5] for details), the above offline-online stages have a few extra steps, the cost of which should be compensated by the superior accuracy of the nonlinear ROM.

For the online phase, the literature offers three different techniques to compute the spatial transform φ_m and the reduced solution u_m .

1. *The data-driven approach* that computes both φ_m and u_m via some linear/nonlinear interpolation and discards the underlying PDE [33].
2. *The semi-PDE approach* that computes φ_m in a data-driven manner but computes u_m using the PDE [16, 18, 30].
3. *The PDE approach* that computes both φ_m and u_m using the PDE [6, 28].

We consider the semi-PDE approach. We use a Lagrange polynomial interpolation and residual minimization to compute φ_m and u_m , respectively. The following reasons motivate our choice. (i) We suspect that by discarding the PDE in the online phase, one might miss out on some physics of the problem, resulting in inaccuracies—similar is the motivation behind physics-based neural networks, which, to enhance the accuracy, impose PDE based constraints on the data-driven nonlinear regression problems [23]. (ii) As [28] suggests, for a purely PDE based approach, one might need the characteristic curves of the PDE to compute φ_m . A characteristics based approach can result in a highly accurate φ_m but its complexity can limit it to one-dimensional problems.

As for the offline phase, to compute the solution snapshots, we use a first-order finite-volume and an explicit Euler time-stepping scheme. To compute the snapshots of the spatial transform, we assume that $\varphi(\cdot, z, \hat{z})$ is a spatial shift function i.e.,

$$(1.4) \quad \varphi(\cdot, z, \hat{z}) = \Theta[c(z, \hat{z})] \text{ where } \Theta[c(z, \hat{z})](x) := x - c(z, \hat{z}), \quad \forall z, \hat{z} \in \mathcal{Z}.$$

We compute the spatial shift $c(z, \hat{z}) \in \mathbb{R}^d$ via L2-minimization [27]. We acknowledge that the above ansatz has limited applicability. As the numerical experiments (and the discussion in [33] and Appendix A.1) indicate, its applicability is limited to problems with a single large discontinuity or to multiple discontinuities moving with the same velocity. To cater to a broader class of problems, we will require a more sophisticated φ than that considered above—a few example can be found in [18, 26, 33, 34]. We provide an extension of our work to such a general φ . However, performing numerical experiments with a different φ than above is left as a part of our future work.

1.2 Residual minimization Performing residual minimization in the online phase is (at least) as expensive as computing the FOM [7, 18]. This is undesirable because despite the availability of an accurate nonlinear approximation space, our ROM will be inefficient. To reduce the computational cost, we perform residual minimization on an online-adaptive reduced mesh, where a reduced mesh refers to a subset of the full mesh. The online-adaptivity allows the reduced mesh to change with the parameter. This accounts for the transport-type behaviour of the residual induced by the nonlinearity of the approximation space $\mathcal{X}_m(z)$. We emphasize that the transport-type behaviour is the reason why the standard non-adaptive reduced mesh techniques (considered in [2, 3, 7]) are ineffective—numerical experiments will provide further elaboration.

An offline/online strategy computes the reduced mesh. The offline phase—using any of the techniques from [2, 3, 7]—collects snapshots of the residual and uses them to compute a reduced mesh. The online phase, capturing the transport in the residual, transports/moves the reduced mesh along the spatial domain. We show that this online phase is efficient on a Cartesian mesh and on an unstructured mesh super-imposed on an auxiliary Cartesian mesh, the so-called structured auxiliary mesh (SAM) [21]. Note that here, efficiency refers to the scaling of the computational cost with the size of the reduced mesh and not with the dimension of the FOM.

Even for the simple spatial transform given above in (1.4), to the best of our knowledge, there do not exist hyper-reduction techniques that perform an efficient

residual minimization for the nonlinear reduction of hyperbolic problems. In [14], authors propose an auto-encoder based nonlinear approximation and use residual minimization to compute a ROM, but do not cater to making the residual minimization efficient. In [18], authors use a fixed non-adaptive reduced mesh to speed-up residual minimization. However, due to the transport-type behaviour of the residual, at least for the test cases that we consider, such an approach is inefficient. In [6], authors propose to speed-up residual minimization via a fast computation of the (L2) inner-products. However, due to a lack of numerical evidence, it is unclear whether this technique results in a significant speed-up.

We note that (similar to [18, 25, 33]) our method is Eulerian as opposed to the Lagrangian methods considered in [19, 29, 30]. In the Lagrangian methods, using the spatial transform φ , one can express the parametrized PDE in the Lagrangian coordinates and reduce the resulting equation using standard techniques. A comparison of the Eulerian methods to the Lagrangian ones is left as a part of our future work. Nonetheless, we point out that expressing the PDE in Lagrangian coordinates introduces space-time gradients of the spatial transform φ . We speculate that ill-conditioned gradients can lead to stability issues in the Lagrangian methods and that no such stability issues should arise with the Eulerian methods. Further rigorous investigation is needed to examine our speculation.

Apart from snapshot transformation, other techniques to construct a nonlinear approximation space include the use of auto-encoders [14], the embedding of the solution manifold in a Wasserstein metric space [10], the online adaptivity of basis [12, 20], and the method of freezing [17, 19]. We leave an exhaustive comparison to these other techniques as a part of our future work.

1.3 Organisation We have organized the rest of the article as follows. [Section 2](#) presents our FOM. The discussion is a brief recall of the standard first-order finite-volume methods. [Section 3](#) presents our ROM. We discuss the sampling of the parameter domain, we concretely define the transformed snapshot based approximation space, we present the residual minimization technique and explain the reason behind its complexity scaling with the dimension of the FOM. [Section 4](#) presents a online-adaptive reduced mesh technique to speed-up residual minimization. This technique attempts to make our ROM more efficient than the FOM. [Section 5](#) provides a rationale behind adapting the reduced mesh, and it extends our technique to structured auxiliary meshes (SAMs) and to spatial transforms different than shifting. [Section 6](#) present numerical examples showcasing the accuracy of our method.

2 Full-order model (FOM) To compute our FOM, we consider an explicit Euler time-stepping scheme and a first-order finite-volume (FV) spatial discretization. The details are as follows. For a parametrized hyperbolic conservation law, the differential operator \mathcal{L} appearing in (1.1) is given as

$$(2.1) \quad \mathcal{L}(\cdot, z) = \nabla \cdot f(\cdot, z) \quad \forall z \in \mathcal{Z}.$$

The flux-function $f(\cdot, z) : \mathbb{R} \rightarrow \mathbb{R}^d$ is assumed to be convex and at least twice-differentiable. For all $(x, \mu) \in \mathbb{R}^d \times \mathcal{P}$, the initial conditions read $u(x, t = 0, \mu) = u_0(x, \mu)$. We assume that $u_0(\cdot, \mu)$ is compactly supported. As a result, due to a finite speed of propagation, for any finite final time T , the solution $u(\cdot, z)$ is also compactly supported. Therefore, we consider a bounded and connected spatial domain $\Omega \subset \mathbb{R}^d$, which, for all $z \in \mathcal{Z}$, contains the support of $u(\cdot, z)$. Along the boundary $\partial\Omega$ and for all $z \in \mathcal{Z}$, we prescribe $u(\cdot, z) = 0$.

A discretization of the space-time domain is as follows. We consider a two-dimensional square spatial domain¹ i.e., $d = 2$ and $\Omega = [0, 1]^2$. We consider $N_x \in \mathbb{N}$ number of mesh elements in each spatial direction, resulting in a grid-size of $\Delta x := 1/N_x$. To discretize the time-domain D , we consider the discrete time-steps $\{t_k\}_{k=0, \dots, K}$ ordered such that

$$(2.2) \quad 0 = t_0 < t_1 \cdots < t_K = T.$$

For simplicity, we consider a constant time-step of Δt .

An explicit Euler time stepping scheme and a FV spatial discretization of the evolution equation (1.1) provides

$$(2.3) \quad U(t_{k+1}, \mu) = U(t_k, \mu) + \Delta t \times \mathcal{F}(U(t_k, \mu)), \quad \forall k \in \{0, \dots, K-1\}, \mu \in \mathcal{P}.$$

The vector $U(t_k, \mu) \in \mathbb{R}^N$ collects the FV degrees-of-freedom of our FOM. Note that for our FV discretization, $N = N_x^2$. The operator $\mathcal{F} : \mathbb{R}^N \rightarrow \mathbb{R}^N$ is a result of a FV discretization and its explicit expression can be found in any standard textbook (for instance, [15]) on FV methods. As the numerical flux (contained in \mathcal{F}), we choose the Local-Lax-Friedrich (LLF) flux—a different choice does not change the forthcoming discussion. We choose the time-step Δt to satisfy the CFL-condition

$$(2.4) \quad \Delta t \leq \frac{\Delta x}{\sup_{x \in \Omega, z \in \mathcal{Z}} 2|\partial_u f(u, z)|_{u=u_N(x, z)}}.$$

Under the assumption that for all $\mu \in \mathcal{P}$, $u_0(\cdot, \mu) \in L^\infty(\Omega)$, the CFL-condition ensures that our FOM is L^∞ stable [11].

3 Reduced-order model (ROM) We recall and elaborate on the summary of the offline and the online phases presented in the introduction, the related details are discussed later.

3.1 Summary: Offline phase The offline phase consists of the following steps.

1. Collect the parameter samples $\{z^{(i)}\}_{i=1, \dots, m} \subset \mathcal{Z}$. We sample the parameter domain uniformly, the details are given in [Subsection 3.3](#).
2. Compute the solution snapshots at the parameter samples.
3. Compute the snapshots of the spatial transform $\{\varphi(\cdot, z^{(j)}, z^{(i)})\}_{i, j}$. As we made the spatial shift ansatz (1.4), we will compute the snapshots of the shifts $\{c(z^{(j)}, z^{(i)})\}_{i, j}$ —[Appendix A.1](#) outlines the technique. The technique builds upon the L2-minimization techniques developed earlier in [18, 27, 30, 33].

3.2 Summary: Online phase For a target parameter $z = (t, \mu) \notin \{z^{(i)}\}_i$, the following steps of the online phase compute a reduced approximation $u_m(\cdot, z)$.

1. *Introduce discrete time-steps:* Consider the discrete time-steps $0 = t_0 < \dots < t_{K^*} = t$. Same as the FOM, consider a constant time-step size of Δt . For simplicity, we do not explore the possibility of a different time-step for the ROM; see [6] for details. For each $t_k \in \{t_j\}_j$, perform the following steps.

¹The differences arising from a non-Cartesian discretization of a square domain are outlined later. An extension to a cuboid discretized with a Cartesian mesh is straightforward. An extension to arbitrary curved domains is left as a part of our future work.

- (a) Approximate $\{\varphi(\cdot, t_k, \mu, z^{(i)})\}_i$ or the shifts $\{c(t_k, \mu, z^{(i)})\}_i$: Using the snapshots of the shifts $\{c(z^{(j)}, z^{(i)})\}_{i,j}$, approximate $\{c(t_k, \mu, z^{(i)})\}_i$ via

$$(3.1) \quad c(t_k, \mu, z^{(i)}) \approx c_m(t_k, \mu, z^{(i)}), \quad \forall i \in \{1, \dots, m\}.$$

To compute $c_m(t_k, \mu, z^{(i)})$, one can use any of the linear/nonlinear regression techniques. With a uniform sampling of the parameter domain (given in [Subsection 3.3](#)), we consider a Lagrange polynomial interpolation/regression. Note that the above approximation of the shift implies

$$\varphi(\cdot, t_k, \mu, z^{(i)}) \approx \varphi_m(\cdot, t_k, \mu, z^{(i)}) = \Theta[c_m(t_k, \mu, z^{(i)})],$$

with Θ being the spatial shift given in [\(1.4\)](#).

- (b) Compute the reduced approximation: find $u_m(\cdot, t_k, \mu)$ in $\mathcal{X}_m(t_k, \mu)$ via residual minimization given as [\[1, 6, 18\]](#)

$$(3.2) \quad \begin{aligned} u_m(\cdot, t_k, \mu) = \arg \min_{v \in \mathcal{X}_m(t_k, \mu)} & \|v - u_m(\cdot, t_{k-1}, \mu) \\ & + \Delta t \times \mathcal{L}_N(u_m(\cdot, t_{k-1}, \mu), t_{k-1}, \mu)\|_{L^2(\Omega)}. \end{aligned}$$

We initialize with $u(t_0, \mu) = \arg \min_{v \in \mathcal{X}_m(t_0, \mu)} \|v - u_0(\cdot, \mu)\|_{L^2(\Omega)}$. The approximation space $\mathcal{X}_m(t_k, \mu)$ is given in [\(1.2\)](#). The operator \mathcal{L}_N approximates the evolution operator \mathcal{L} . Its precise form is not important here, and we discuss the details in [Subsection 3.4](#). As [Subsection 3.5](#) clarifies, the complexity of solving the above problem scales with the dimension of the FOM therefore, we later equip it with hyper-reduction.

REMARK 1 (Computing the projection operator Π). *On a Cartesian mesh, we define Π (given in [\(1.2\)](#)) by approximating the shifts by an integer multiple of Δx . This provides*

$$(3.3) \quad \begin{aligned} & \Pi(\text{span}\{u_N(\Theta[c_m(t_k, \mu, z^{(i)})], z^{(i)})\}_{i \in \Lambda(t_k, \mu)}) \\ & := \text{span}\{u_N(\Theta \left[\left\lfloor \frac{c_m(t_k, \mu, z^{(i)})}{\Delta x} \right\rfloor \Delta x \right], z^{(i)})\}_{i \in \Lambda(t_k, \mu)}, \end{aligned}$$

where $\lfloor n \rfloor$ represents the greatest integer less than equal to n . One can check that the space on the right is included in \mathcal{X}_N . The above definition is faster to compute than an orthogonal projection operator, which requires a numerical quadrature routine. However, on a general unstructured mesh, the above space on the right is not necessarily included in \mathcal{X}_N and we resort to using the orthogonal projection operator. This slightly increase the computation cost of the algorithm, [Subsection 5.3](#) discusses the details.

REMARK 2 (Boundary conditions for shifting). *For $x \notin \Omega$ and some shift $c^* \in \mathbb{R}^d$, we define $\Theta[c^*](x) = 0$, which is consistent with the fact that $u(\cdot, z)$ is compactly supported in Ω .*

3.3 Sampling the parameter domain We consider a two-dimensional parameter domain \mathcal{Z} —an extension to higher dimensions is straightforward. We assume that \mathcal{Z} is (or can be mapped via a bijection to) a rectangle. We take N_t and N_μ uniformly placed samples from D and \mathcal{P} , respectively. The vertices of \mathcal{Z} are included in the samples, and the samples from D are a subset of the time-instances $\{t_k\}_{k=0, \dots, K}$ used to compute the FOM. To collect the samples from \mathcal{Z} , we take a tensor-product of the samples in D and \mathcal{P} .

REMARK 3 (Scaling with p). *Uniform sampling can make snapshot computation unaffordable for large values of p . In that case, one can consider a greedy/sparse sampling technique [9, 22].*

3.3.1 Neighbours under uniform sampling Figure 1 shows the parameter samples that we identify as the neighbours of a parameter. This provides the index set $\Lambda(z)$ appearing in the approximation space $\mathcal{X}_m(z)$ given in (1.2). A uniform sampling of \mathcal{Z} induces a structured mesh of $(N_t - 1) \times (N_\mu - 1)$ parameter elements. Each parameter $z \in \mathcal{Z}$ belongs to either a parameter element or to its boundary—generically, we denote the parameter element by $\mathcal{I}^{\mathcal{Z}}$ and collect its definition below. In the first case, the vertices of $\mathcal{I}^{\mathcal{Z}}$ are the neighbours of z , whereas in the latter case, the vertices of $\mathcal{I}^{\mathcal{Z}}$ closest to z are its neighbours.

DEFINITION 3.1 (Representative element $\mathcal{I}^{\mathcal{Z}}$). *We define $\mathcal{I}^{\mathcal{Z}}$ as $\mathcal{I}^{\mathcal{Z}} := (t_1^*, t_2^*) \times (\mu_1^*, \mu_2^*)$, where t_i^* and μ_i^* are some elements of D and \mathcal{P} , respectively. The vertices of $\mathcal{I}^{\mathcal{Z}}$ are given—in a counter-clockwise fashion—as $z_*^{(1)} = (t_1^*, \mu_1^*)$, $z_*^{(2)} = (t_2^*, \mu_1^*)$, $z_*^{(3)} = (t_2^*, \mu_2^*)$, and $z_*^{(4)} = (t_1^*, \mu_2^*)$.*

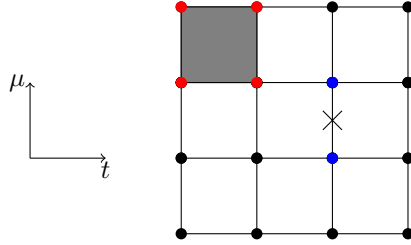


Fig. 1: Bold dots: uniform samples. Red dots: neighbours for parameters inside the gray region. Blue dots: neighbours for parameters at the crossed-out edge.

REMARK 4 (The locality of the approximation space $\mathcal{X}_m(z)$). *Consider a $z \in \mathcal{I}^{\mathcal{Z}}$. With our sampling of the parameter domain, the approximation space $\mathcal{X}_m(z)$ in (1.2) transforms to*

$$(3.4) \quad \mathcal{X}_m(z) = \Pi(\text{span}\{u_N(\varphi_m(\cdot, z, z_*^{(i)}), z_*^{(i)})\}_{i=1,\dots,4}).$$

The space $\mathcal{X}_m(z)$ (and also the one considered in [18]) is local—it only uses parameter samples that lie in some neighbourhood of the target parameter. This is consistent with the observation (see [1, 18]) that, eventually, only the snapshots with parameters that lie in the neighbourhood of z contribute to the approximation of $u_N(\cdot, z)$ —the expansion coefficients for all the other snapshots are negligible.

3.4 Residual Minimization Interpreting the FOM given in (2.3) as a residual minimization problem provides

$$(3.5) \quad U(t_{k+1}, \mu) = \arg \min_{w \in \mathbb{R}^N} \|\text{Res}(w, U(t_k, \mu))\|_{l_2}^2, \quad \forall \mu \in \mathcal{P}.$$

The residual $\text{Res} : \mathbb{R}^N \times \mathbb{R}^N \rightarrow \mathbb{R}^N$ follows from the FOM (2.3) and is given as

$$(3.6) \quad \text{Res}(w, v) := w - v - \Delta t \times \mathcal{F}(v).$$

Obviously, $\text{Res}(w, U(t_k, \mu)) = 0$ for $w = U(t_{k+1}, \mu)$.

We use the above formulation of the FOM to design a time-stepping scheme for our ROM. Let $z \in \mathcal{I}^{\mathcal{Z}}$, where $\mathcal{I}^{\mathcal{Z}}$ is the parameter element in [Definition 3.1](#). The approximation space $\mathcal{X}_m(z)$ is isomorphic to $\text{range}(A(z))$. The matrix $A(z)$ is of size $N \times 4$ and contains shifted snapshots as its columns. Equivalently,

$$(3.7) \quad A(z) := \left(\mathcal{T} \left[c_m(z, z_*^{(1)}) \right] U(z_*^{(1)}), \dots, \mathcal{T} \left[c_m(z, z_*^{(4)}) \right] U(z_*^{(4)}) \right).$$

For some shift $c^* \in \mathbb{R}^d$, the operator $\mathcal{T}[c^*] : \mathbb{R}^N \rightarrow \mathbb{R}^N$ shifts a snapshot along the spatial domain—a precise definition is given below ([Definition 3.2](#)).

To compute our ROM, instead of minimizing the residual (given in [\(3.5\)](#)) over \mathbb{R}^N , we minimize it over the reduced approximation space $\text{range}(A(t_{k+1}, \mu))$. This provides the time-stepping scheme

$$(3.8) \quad U_m(t_{k+1}, \mu) = \arg \min_{w \in \text{range}(A(t_{k+1}, \mu))} \|\text{Res}(w, U_m(t_k, \mu))\|_{l^2}^2, \quad \forall \mu \in \mathcal{P}.$$

We initialize with $U_m(t_0, \mu) := \arg \min_{w \in \text{range}(A(t_0, \mu))} \|w - U(t_0, \mu)\|_{l^2}$.

DEFINITION 3.2 (Shift operator). *Let $v \in \mathbb{R}^N$ contain the FV degrees-of-freedom of a function $g : \mathbb{R}^d \rightarrow \mathbb{R}$ compactly supported inside Ω . Then, with $\mathcal{T}[c^*]v \in \mathbb{R}^N$ we denote a vector that contains the FV degrees-of-freedom of the shifted and projected function $\Pi(g(\Theta[c^*]))$, with Π as given in [Remark 1](#).*

3.4.1 Least-squares formulation Since $U_m(t_{k+1}, \mu) \in \text{range}(A(t_{k+1}, \mu))$, we find

$$(3.9) \quad U_m(t_{k+1}, \mu) = A(t_{k+1}, \mu)\alpha(t_{k+1}, \mu),$$

where $\alpha(t_{k+1}, \mu) \in \mathbb{R}^4$. With the above relation, the minimization problem [\(3.8\)](#) transforms to a least-squares problem

$$(3.10) \quad \alpha(t_{k+1}, \mu) = \arg \min_{y \in \mathbb{R}^4} \|A(t_{k+1}, \mu)y - b(t_k, \mu)\|_{l^2}^2,$$

with the vector $b(t_k, \mu) \in \mathbb{R}^N$ given as

$$(3.11) \quad b(t_k, \mu) := U_m(t_k, \mu) + \Delta t \times \mathcal{F}(U_m(t_k, \mu)).$$

Consider the underlined vector in the above problem [\(3.10\)](#). The i -th element of this vector represents the residual in the i -th mesh element. Since we take the l^2 -norm of the entire vector, we minimize the residual over the entire mesh. To highlight this fact, we reformulate the above problem. We collect element ids in the set $\mathcal{E}_z \subseteq \mathcal{E}_{full}$, where

$$\mathcal{E}_{full} := \{1, \dots, N\}.$$

The subscript $z \in \mathcal{Z}$ signifies that \mathcal{E}_z can change with the parameter. Furthermore, with \mathcal{E}_z , we can identify any subset of the spatial mesh. We refer to this subset as the reduced mesh—[Figure 2](#) shows a sample reduced mesh. For simplicity, we assume that the size of \mathcal{E}_z is z -independent and denote it by

$$(3.12) \quad \#\mathcal{E}_z = n.$$

Obviously, $n \leq N$.

In the following, we define sub-matrices with rows indexed by the entries in \mathcal{E}_z .

DEFINITION 3.3 (Sub/Reduced-matrices). *Let $V(y) \in \mathbb{R}^{N \times n_2}$, with y belonging to some set \mathcal{Y} . With $V[\mathcal{E}_z](y)$ we denote a $n \times n_1$ matrix that contains the n -rows of $V(y)$ indexed by \mathcal{E}_z i.e.,*

$$(3.13) \quad (V[\mathcal{E}_z](y))_{ij} := (V(y))_{ij}, \quad \forall i \in \mathcal{E}_z, j \in \{1, \dots, n_2\}.$$

With the list \mathcal{E}_z and the above notation, we can choose the mesh elements over which we minimize the residual. The quantity $A[\{i\}](t_{k+1}, \mu)y - b[\{i\}](t_k, \mu)$ denotes the residual in the i -th mesh element—same as the i -th entry of the underlined vector in (3.10). Thus, to minimize the residual over a reduced mesh identified with a list \mathcal{E}_z , we compute

$$(3.14) \quad \begin{aligned} \alpha(t_{k+1}, \mu) &= \arg \min_{y \in \mathbb{R}^4} \sum_{i \in \mathcal{E}_{t_{k+1}, \mu}} |A[\{i\}](t_{k+1}, \mu)y - b[\{i\}](t_k, \mu)|^2, \\ &= \arg \min_{y \in \mathbb{R}^4} \|A[\mathcal{E}_{t_{k+1}, \mu}](t_{k+1}, \mu)y - b[\mathcal{E}_{t_{k+1}, \mu}](t_k, \mu)\|_{l^2}^2. \end{aligned}$$

The second equality is nothing but the definition of the l^2 -norm. Figure 2 further elaborates on the above minimization problem. To minimize the residual over the entire mesh—and recover the earlier least-squares problem (3.10)—one can choose $\mathcal{E}_{t, \mu} = \mathcal{E}_{full}$, for all $(t, \mu) \in \mathcal{Z}$.

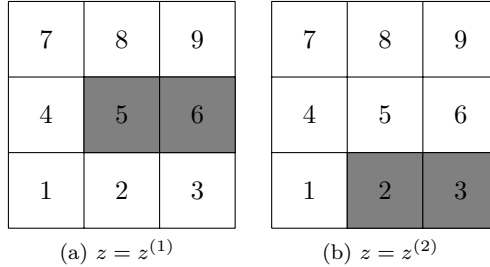


Fig. 2: A mesh with $N = 9$ elements. The reduced mesh is a union of the gray elements. It can change with the parameter, which we refer to as online-adaptivity. With $\mathcal{E}_z = \{1, \dots, 9\}$, in (3.14) we compute the residual on the entire mesh. Whereas, for (a), with $\mathcal{E}_z = \{5, 6\}$, we compute the residual only on the reduced mesh.

3.5 Computational cost We study the cost of computing the above least-squares problem. To both compute and minimize the residual, we require $\mathcal{O}(n)$ operations, where $n = \#\mathcal{E}_z$. To minimize the residual, we consider the `lsqminnorm` routine from `matlab`, which provides the minimum-norm solution and requires $\mathcal{O}(n)$ operations. Furthermore, to compute the residual, we compute:

1. The index set $\mathcal{E}_{t_{k+1}, \mu}$, in case it changes with t_{k+1}, μ . Otherwise—like for the above choice of \mathcal{E}_z —we can compute and store $\mathcal{E}_{t_{k+1}, \mu}$ offline.
2. The matrix containing the shifted snapshots $A[\mathcal{E}_{t_{k+1}, \mu}](t_{k+1}, \mu)$.
3. The vector $b[\mathcal{E}_{t_{k+1}, \mu}](t_k, \mu)$.

For our online-adaptive technique discussed later (in Subsection 4.2.2), the first step requires $\mathcal{O}(n)$ operations. Furthermore, the other two steps also have $\mathcal{O}(n)$ complexity. Two basic operations determine this complexity (i) the shifted snapshot computation, and (ii) the computation of the action of the operator \mathcal{F} . We study the complexity of both these operations.

3.5.1 Cost of computing a shifted snapshot and \mathcal{F} The routine in [Algorithm 3.1](#) computes the shifted snapshot $\mathcal{T}[c^*]U[\mathcal{E}_z](z)$. Owing to [Remark 1](#), we restrict to a shift c^* that is an integer multiple of Δx . As a result, $\mathcal{T}[c^*]U[\mathcal{E}_z](z)$ is related to $U[\mathcal{E}_z](z)$ via the relation given in [line-8](#) and its computation requires the id of the cell that contains the shifted centre. We compute this id via the `get_location_id` routine given in [Algorithm 3.2](#). The `get_location_id` routine requires $\mathcal{O}(1)$ operations thus, [Algorithm 3.1](#) requires $\mathcal{O}(n)$ operations.

To compute $b[\mathcal{E}_z](z)$, we require the discreet evolution operator $\mathcal{F}[\mathcal{E}_z](U_m(z))$. To compute this operator, for each cell in \mathcal{E}_z , we perform the following operations (i) find the neighbouring cells; (ii) compute the numerical flux at every face; and (iii) integrate the numerical flux along the cell boundary. On a Cartesian mesh, each of these operations have $\mathcal{O}(1)$ complexity. Thus, for the n entries in \mathcal{E}_z , we require $\mathcal{O}(n)$ operations to compute $\mathcal{F}[\mathcal{E}_z](U_m(z))$.

Algorithm 3.1 Algorithm to compute a shifted snapshot

```

1: Input  $U[\mathcal{E}_z](z)$ ,  $c^*$ ,  $\mathcal{E}_z$ ,  $N_x$ ,  $\Delta x$ 
2: Output  $\mathcal{T}[c^*]U[\mathcal{E}_z](z)$ 
3:  $k \leftarrow 1$ 
4: for  $i \in \mathcal{E}_z$  do
5:    $x_i \leftarrow \text{get\_cell\_centre}(i) - c^*$  {The shifted cell center}
6:   if  $x_i \in \Omega$  then
7:      $j \leftarrow \text{get\_location\_id}(x_i, N_x, \Delta x)$  {Values from inside of  $\Omega$ }
8:      $(\mathcal{T}[c^*]U[\mathcal{E}_z](z))_k = (U[\mathcal{E}_z](z))_j$ 
9:   else
10:     $(\mathcal{T}[c^*]U[\mathcal{E}_z](z))_k = 0$  {Prescribe boundary conditions}
11:   end if
12:    $k \leftarrow k + 1$ 
13: end for

```

Algorithm 3.2 `get_location_id`: given the location of a space point, computes the id of the mesh element that contains it.

```

1: Input  $x \in \mathbb{R}^2$ ,  $N_x$ ,  $\Delta x$ 
2: Output element_id
3:  $\text{id}_x \leftarrow \text{mod}(x(1), \Delta x)$ 
4:  $\text{id}_y \leftarrow \text{mod}(x(2), \Delta x)$ 
5:  $\text{element\_id} \leftarrow (\text{id}_y - 1) \times N_x + \text{id}_x$ 

```

4 Hyper-reduction With $\mathcal{E}_z = \mathcal{E}_{full}$, our ROM is (at least) as expensive as the FOM, which is undesirable. While maintaining the accuracy of the ROM, we want to choose \mathcal{E}_z such that $n \ll N$. This way, one can expect the ROM to be more efficient than the FOM. We pursue two approaches to compute such a \mathcal{E}_z .

1. *The non-adaptive technique* that keeps \mathcal{E}_z fixed in the parameter space.
2. *The online-adaptive technique* where \mathcal{E}_z changes with the parameter i.e., the index set \mathcal{E}_z is online-adaptive.

First, we present the non-adaptive technique and its shortcomings.

4.1 Non-adaptive technique This technique consists only of an offline phase. At $\{\bar{\mu}_j\}_{j=1, \dots, m_{hyp}} \in \mathcal{P}$ parameter samples, we solve the non-hyper-reduced least-

squares problem in (3.10) and collect snapshots of the residuals. This provides the snapshot matrix

$$(4.1) \quad \mathcal{S} := (\text{Res}(U_m(t_2, \bar{\mu}_1), U_m(t_1, \bar{\mu}_1)), \text{Res}(U_m(t_3, \bar{\mu}_1), U_m(t_2, \bar{\mu}_1)), \dots, \text{Res}(U_m(t_K, \bar{\mu}_{m_{hyp}}), U_m(t_{K-1}, \bar{\mu}_{m_{hyp}}))).$$

To compute \mathcal{E}_z , the non-adaptive technique applies Algorithm 4.1 (or any other point-selection algorithm from [3, 7]) to \mathcal{S} . The algorithm (taken from [2]) selects the mesh elements with the largest l^2 -norm of the residual taken over all the parameter samples. Note that as compared to [2], we apply the algorithm directly to \mathcal{S} and not to its POD modes. Numerical experiments suggest that both the strategies provide similar results.

Algorithm 4.1 Summary of the reduced mesh selection algorithm from [2]

- 1: **Input** \mathcal{S}, n
 - 2: **Output** \mathcal{E}_z
 - 3: **for** $i \in \{1, \dots, N\}$ **do**
 - 4: $r(i) = \|\mathcal{S}(i, :)\|_2$ { $\mathcal{S}(i, :)$ denotes the i -th row of \mathcal{S} . }
 - 5: **end for**
 - 6: $[\mathbf{r_sorted}, idx] = \text{sort}(r)$ {Sort in decreasing order and $\mathbf{r_sorted} = r(idx)$.}
 - 7: $\mathcal{E}_z \leftarrow idx(1 : n)$
-

4.1.1 Shortcomings Our numerical experiments (and the example below) suggest that the non-linearity of the approximation space $\mathcal{X}_m(z)$ induces a transport-type behaviour in the residual. As a result, only a large reduced mesh computed using Algorithm 4.1 can provide a reasonable accuracy—a similar observation holds for the other point-selection techniques outlined in [3, 7]. This is undesirable because, at least ideally, for some error tolerance of practical interest ($\|u_N(\cdot, z) - u_m(\cdot, z)\|_{L^2} \leq \text{TOL}$, for instance), the size of the reduced mesh should be as small as possible. Algorithm 4.1 provides a parameter-independent reduced mesh, which might not be accurate for the entire range of the parameter domain when the residual shows a transport-type behaviour. Indeed, the motivation to introduce parameter-dependence in the approximation space $\mathcal{X}_m(z)$ was to well-approximate the transport type behaviour of the solution. A parameter-independent linear approximation space (a span of the POD basis, for instance) cannot achieve this task. For further elaboration, consider the example below. The example considers a moving step function and discusses the shortcomings of a non-adaptive reduced mesh.

EXAMPLE 4.1 (Non-adaptive reduced mesh for a moving characteristic function).

Consider $g(\cdot, z) = (1 + z^2)\mathbb{1}_{[z-0.2, z]}$, where $\mathbb{1}_A$ represents a characteristic function over a set $A \subset \mathbb{R}$. Let $z \in \mathcal{Z} = [0, 2]$, and sample \mathcal{Z} at $z^{(1)} = 0$ and $z^{(2)} = 2$. We approximate $g(\cdot, z)$ by $g_m(\cdot, z) \in \text{span}\{g(\Theta[c(z, z^{(i)})], z^{(i)})\}_{i=1,2}$ with $c(z, z^{(i)}) = z - z^{(i)}$. To compute $g_m(\cdot, z)$, we perform a linear interpolation between the transformed snapshots $g(\Theta[c(z, z^{(1)})], z^{(1)})$ and $g(\Theta[c(z, z^{(2)})], z^{(2)})$, which results in the error

$$(4.2) \quad E(\cdot, z) := |g(\cdot, z) - g_m(\cdot, z)| = z(2 - z)\mathbb{1}_{[z-0.2, z]}.$$

We interpret $E(\cdot, z)$ as a residual. Note that, similar to $g(\cdot, z)$, the residual also shifts to the right as z increases, exhibiting a transport-type behaviour.

We consider $N = 2 \times 10^3$ grid points inside $[-2, 2]$, and collect snapshots of $E(\cdot, z)$ at 5 uniformly placed (excluding the endpoints) parameter samples $\{\bar{z}^{(i)}\}_{i=1, \dots, 5}$ inside \mathcal{Z} . This provides the snapshot matrix $\mathcal{S}_{ij} = E(x_i, \bar{z}^{(j)})$. Figure 3 shows these snapshots. We compute a reduced mesh of size $n = 100$ using Algorithm 4.1. The locations of the centres of a few of the reduced mesh elements, over-plotted on a few of the snapshots of the error (different from those contained in \mathcal{S}), are shown in Figure 3. We make the following observations. (i) Obviously, the reduced mesh does not change with z . (ii) For all the three snapshots (and also for the several others not shown in the plot), none of the reduced mesh elements lie inside the support of the residual. For a residual minimization based technique, this could either result in a trivial ROM (i.e., $u_m = 0$) or, as the later numerical experiments indicate, can make the ROM unstable. (iv) At least 800 mesh elements are needed to have at least one reduced mesh element inside the support of $E(\cdot, z)$ for every $z \in \mathcal{Z}$. Note that 800 is 40% of the total number of grid points N . For such a large reduced mesh, we do not expect to achieve a significant speed-up as compared to the non-hyper-reduced residual minimization.

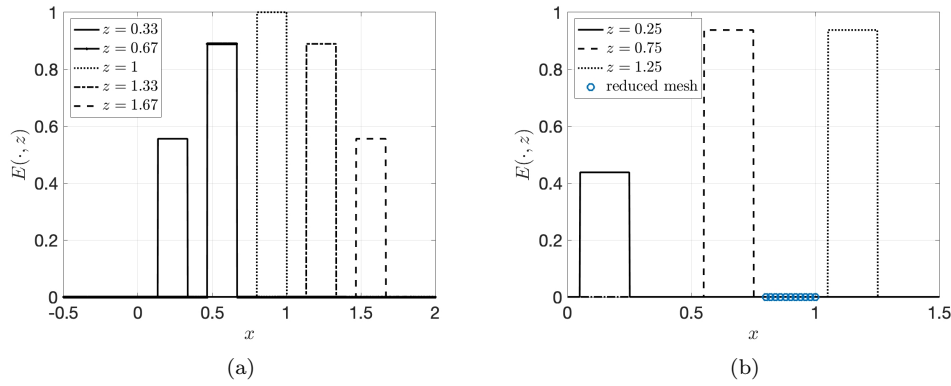


Fig. 3: Results for Example 4.1. (a) Snapshots used to compute the reduced mesh. (b) A few snapshots of the residual—different from those used to compute the reduced mesh—and the cell centres of the reduced mesh. The reduced mesh is localized around the support of the snapshot at $z = 1$.

4.2 Online-adaptive technique To account for the transport-type behaviour of the residual, we introduce online-adaptivity in the reduced mesh. This results in an online and an offline stage that computes \mathcal{E}_z ; below is a brief summary. The matrix \mathcal{S} is the snapshot matrix given in (4.1). The details of the two stages are given later.

$$(4.3) \quad \begin{aligned} \text{Offline Phase : } & \mathcal{S} \xrightarrow[\text{residuals}]{\text{shift}} \mathcal{S}_{\text{shift}} \xrightarrow[\text{reduced mesh}]{\text{select}} \mathcal{E}_{\text{off}} \subseteq \{1, \dots, N\}. \\ \text{Online Phase : } & \mathcal{E}_{\text{off}} \xrightarrow[\text{reduced mesh}]{\text{adapt}} \mathcal{E}_z. \end{aligned}$$

To select the reduced mesh in the offline phase, we use Algorithm 4.1—any other point selection techniques outlined in [2, 3, 7, 18] will also suffice.

4.2.1 Offline stage Similar to the solution, we transform the snapshots of the residuals by evaluating them on a transformed spatial domain—in the language of [27], this reverses the effect of transport in the residuals. For reasons made clear later in [Subsection 5.1](#), a transformation based on shifting is sufficient. This provides a snapshot matrix of shifted residuals given as

$$(4.4) \quad \mathcal{S}_{shift} := (\mathcal{T}[-c_m(t_2, \bar{\mu}_1, z_{ref})] \text{Res}(U_m(t_2, \bar{\mu}_1), U_m(t_1, \bar{\mu}_1)), \dots, \mathcal{T}[-c_m(t_K, \bar{\mu}_{m_{hyp}}, z_{ref})] \text{Res}(U_m(t_K, \bar{\mu}_{m_{hyp}}), U_m(t_{K-1}, \bar{\mu}_{m_{hyp}}))).$$

Above, z_{ref} could be any of the $N_\mu \times N_t$ parameter samples taken from \mathcal{Z} —refer back to [Subsection 3.3](#) for details. Furthermore, [Algorithm 3.1](#) provides the shifted residuals, and the shifts $\{c_m(t_i, \bar{\mu}_j, z_{ref})\}_{i,j}$ result from a Lagrange polynomial interpolation over the shift snapshots $\{c(z^{(i)}, z^{(j)})\}_{i,j}$.

After reversing the effect of transport in the residuals, we apply [Algorithm 4.1](#) to \mathcal{S}_{shift} . This results in a reduced mesh with the ids contained in \mathcal{E}_{off} . The online phase adapts this reduced mesh.

4.2.2 Online stage The two steps below constitute the `adapt_reduced_mesh` routine appearing in the online phase of (4.3). The rationale behind these two steps is described below. We perform these steps for each of the entries in \mathcal{E}_{off} .

1. Compute the cell center x_c of a cell contained in \mathcal{E}_{off} .
2. Using the `get_location_id` routine given in [Algorithm 3.2](#), find the cell id containing the shifted point $x_c + c_m(t_{k+1}, \mu, z_{ref})$. Include this cell id in $\mathcal{E}_{t_{k+1}, \mu}$.

As noted earlier (in [Subsection 3.5](#)), the `get_location_id` routine requires $\mathcal{O}(1)$ operations. Thus, computing the entries of $\mathcal{E}_{t_{k+1}, \mu}$ requires $\mathcal{O}(n)$ operations.

Following is a rationale justifying the above two steps. We express the un-shifted residual in terms of the shifted residual to find

$$(4.5) \quad \text{Res}(U_m(t_{k+1}, \mu), U_m(t_k, \mu)) = \mathcal{T}[c_m(t_{k+1}, \mu, z_{ref})] \underline{\mathcal{T}[-c_m(t_{k+1}, \mu, z_{ref})] \text{Res}(U_m(t_{k+1}, \mu), U_m(t_k, \mu))}.$$

The entries in \mathcal{E}_{off} represent a reduced mesh where the (underlined) shifted residual is the largest in magnitude. Thus, to have a reduced mesh where the un-shifted residual $\text{Res}(U_m(t_{k+1}, \mu), U_m(t_k, \mu))$ is the largest in magnitude, we shift the centres corresponding to the mesh elements in \mathcal{E}_{off} by $c_m(t_{k+1}, \mu, z_{ref})$.

We revisit [Example 4.1](#) with our online adaptive technique.

EXAMPLE 4.2 (Revisiting [Example 4.1](#)). *The numerical parameters remain the same as earlier. In the offline phase, we apply [Algorithm 4.1](#) to the shifted snapshot matrix $(\mathcal{S}_{shift})_{ij} = E(x_i + \bar{z}^{(j)}, \bar{z}^{(j)})$. This provides \mathcal{E}_{off} . In the online phase, we shift \mathcal{E}_{off} by $z/\Delta x$. The results are shown in [Figure 4](#). The reduced mesh is parameter-dependent and adapts to the residual. As a result, unlike the non-adaptive technique, almost the entire reduced mesh lies inside the support of each residual. In the later numerical experiments, this provides superior accuracy as compared to the non-adaptive technique.*

5 Discussion and extensions

5.1 Why shifting residuals works? We explain why a spatial shift can provide a reasonable transformation of the residual or, equivalently, can reverse the effect of transport in the residual. Under some assumptions (listed below in [Lemma 5.1](#)),

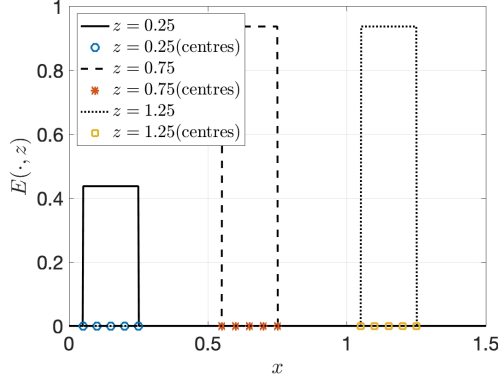


Fig. 4: Revisiting [Example 4.1](#) with the online-adaptive technique. Centres of the online-adapted reduced mesh and the error $E(\cdot, z)$ given in [\(4.2\)](#).

we establish that the shifted residual can be given as

$$(5.1) \quad \mathcal{T}[-c(t_{k+1}, \mu, z_{ref})] \text{Res}(U_m(t_{k+1}, \mu), U_m(t_k, \mu)) = \text{Res}^*(t_k, \mu) + \mathcal{O}(\Delta t),$$

where, as μ and t_k vary over \mathcal{P} and $\{t_j\}_j$, respectively, the function $(t_k, \mu) \mapsto \text{Res}^*(t_k, \mu)$ has no/minimal transport-type behaviour. The above relation indicates that for a sufficiently small Δt , shifting should provide an accurate transformation of the residual.

The following result establishes the above relation, and follows from properties of the shift operator \mathcal{T} , the evolution operator \mathcal{F} and some additional assumptions—[Remark 5](#) further elaborates on the assumptions. For simplicity and for all $z, \hat{z} \in \mathcal{Z}$, we assume that the exact shift values $c(z, \hat{z})$ are known—similar arguments hold for an accurate approximation $c_m(z, \hat{z})$.

LEMMA 5.1. *Assume the following.*

(C1) $c(z, \hat{z}) = -c(\hat{z}, z)$, $\forall z, \hat{z} \in \mathcal{Z}$.

(C2) $c(z, \tilde{z}) = c(z, \hat{z}) + c(\hat{z}, \tilde{z})$, $\forall z, \tilde{z}, \hat{z} \in \mathcal{Z}$.

(C3) $\mathcal{T}[c^*]\mathcal{F}(v) = \mathcal{F}(\mathcal{T}[c^*]v)$. Here, $v \in \mathbb{R}^N$ contains the FV degrees-of-freedom of a function $g: \mathbb{R}^d \rightarrow \mathbb{R}$ whose support is contained inside Ω , c^* is a shift such that the support of the shifted function $g(\Theta[c^*])$ is also contained inside Ω , \mathcal{F} is the evolution operator defined in [\(2.3\)](#), and $\mathcal{T}[c^*]$ is the shift operator in [Definition 3.2](#).

(C4) $\mathcal{F} \in W^{1,\infty}(\mathbb{R}^N)$. Here, $W^{1,\infty}(\mathbb{R}^N)$ represents a Sobolev space of functions defined over \mathbb{R}^N with bounded weak derivatives upto first-order.

(C5) Under the CFL-condition [\(2.4\)](#), with the initial data in L^∞ , and with $\mathcal{E}_z = \mathcal{E}_{full}$, the ROM resulting from the minimization problem [\(3.14\)](#) is L^∞ -stable.

Then, the relation in [\(5.1\)](#) holds with

$$(5.2) \quad \text{Res}^*(t_k, \mu) := \tilde{U}_m(t_{k+1}, \mu) - (\text{Id} + \Delta t \times \mathcal{F})\tilde{U}_m(t_k, \mu),$$

where $\tilde{U}_m(z) = \sum_i \alpha_i(z) \mathcal{T}[c(z_{ref}, z_*^{(i)})] U(z_*^{(i)})$, and α_i is given in [\(3.9\)](#). Furthermore, z_{ref} is the reference parameter appearing in [\(4.1\)](#), and $z_*^{(i)}$ are the vertices of the reference element in [Definition 3.1](#).

Proof. See [Appendix B](#). □

We expect $\text{Res}^*(t_k, \mu)$ to not have a transport dominated behaviour. First, consider $\tilde{U}_m(z)$. It is a linear combination of snapshots taken from the transformed solution set $\{\mathcal{T}[c(z_{ref}, z)]U(z) : z \in \mathcal{Z}\}$. Assuming that shifting provides an accurate snapshot transformation—otherwise, our ROM will be inaccurate—as z varies over \mathcal{Z} , $\tilde{U}_m(z)$ should not exhibit a dominant transport-type behaviour.

Now, consider the second term on the right in [\(5.2\)](#) where the operator $\text{Id} + \Delta t \times \mathcal{F}$ acts on $\tilde{U}_m(z)$. As discussed above, $\tilde{U}_m(z)$ does not exhibit a transport-type behaviour. Furthermore, due to the CFL-condition [\(2.4\)](#), this operator can "move" $U_m(z)$ by a maximum of one grid-cell of size Δx , which, for a sufficiently small Δt and owing to the CFL-condition, is not a dominant transport type behaviour. This justifies our choice to transform the residual with a spatial shift.

REMARK 5 (Comments on the assumptions made in the above result). *(C1) This is an anti-symmetry property and follows from the minimization problem given in [\(A.4\)](#). (C2) This property states that shifting can be performed in steps, which, at least intuitively, seems reasonable [\[33, 34\]](#). The intuition (at least for the test cases that we consider) is justified by numerical experiments. (C3) For compactly supported solutions, this property holds true if the continuous-in-space analogue of \mathcal{F} , i.e., $\nabla \cdot f$ where f is the flux function, commutes with shifting. This commutation property is a weaker version of Galilean invariance that holds true for most hyperbolic equation of practical relevance—examples include the wave equation, Euler equations, Burgers' equation, etc. (C4) For a twice continuously differentiable flux-function and at least for a LLF numerical flux, one can check that this property holds true. (C5) Our assumption states that the ROM inherits the L^∞ stability of the FOM. A rigorous stability proof is unavailable, as yet. Nonetheless, at least for our numerical experiments, the assumption is valid.*

5.2 Extension to a general spatial transform We present an extension of our technique to a general spatial transform $\varphi(\cdot, z, \hat{z}) : \Omega \rightarrow \Omega$, which might or might not be the same as the shift function $\Theta[c^*(z, \hat{z})]$. Such a transform is suitable for problems involving time-dependent boundary conditions, multiple shocks, shock interaction, etc [\[18, 30, 33\]](#).

Let $\mathcal{T}[\varphi]$ be the same as the shift operator $\mathcal{T}[c^*]$ given in [Definition 3.2](#) but with the shift function $\Theta[c^*]$ replaced by a general φ . For most physically relevant PDEs, the evolution operator \mathcal{F} does not need to commute with $\mathcal{T}[\varphi]$ i.e., the assumption (C3) in [Lemma 5.1](#) might not hold true with $\mathcal{T}[c^*]$ replaced by $\mathcal{T}[\varphi]$. As a result, following the previous discussion, transforming the residual with φ might be inaccurate—the transformed residual might still have a dominant transport-type behaviour. Therefore, we need to treat the residual and the solution separately, and find a spatial transform for the residual that is different from that for the solution. This is in contrast to shifting where (thanks to the property (C3)) the same spatial transform, i.e. shifting, is used to transform both the solution and the residual.

For $z, \hat{z} \in \mathcal{Z}$, let $\varphi_R(\cdot, z, \hat{z}) : \Omega \rightarrow \Omega$ represent the spatial transform for the residual—we emphasize that φ_R does not need to be the same as φ . Then, similar to \mathcal{S}_{shift} given in [\(4.4\)](#), we can define the transformed snapshot matrix of residuals as

$$(5.3) \quad \mathcal{S}_{\varphi_R} := (\mathcal{T}[\varphi_R(\cdot, z_{ref}, t_2, \bar{\mu}_1)] \text{Res}(U_m(t_2, \bar{\mu}_1), U_m(t_1, \bar{\mu}_1)), \dots, \mathcal{T}[\varphi_R(\cdot, z_{ref}, t_K, \bar{\mu}_{m_{hyp}})] \text{Res}(U_m(t_K, \bar{\mu}_{m_{hyp}}), U_m(t_{K-1}, \bar{\mu}_{m_{hyp}}))) .$$

Offline, we apply [Algorithm 4.1](#) to \mathcal{S}_{φ_R} and compute \mathcal{E}_{off} . Online, using the routine

`adapt_reduced_mesh` outlined in [Subsection 4.2.2](#), we transform the cell centres of mesh elements whose ids are contained in \mathcal{E}_{off} with the transform $\varphi_R(\cdot, z_{ref}, t_{k+1}, \mu)$. As stated earlier, on a Cartesian mesh, this procedure requires $\mathcal{O}(n)$ operations. Note that, same as for the solution, one can compute φ_R using the non-convex optimization techniques outlined in [\[18, 30, 33\]](#).

5.3 Extension to a Structured Auxiliary Mesh (SAM) We study the computational cost of our ROM technique for a SAM. In a SAM, an unstructured mesh sits atop an auxiliary Cartesian mesh. [Figure 5](#) depicts a simple example, further details can be found in [\[21\]](#). We assume that we have N_{uc} number of unstructured cells in each of the N_{cc} number of Cartesian cells. Thus, the total number of cells read $N = N_{uc} \times N_{cc}$. We assume that N_{uc} is independent of N . We claim that on a SAM our ROM requires $\mathcal{O}(N_{uc}N_{quad}n)$ operations, where N_{quad} is the number of quadrature points per cell, and n is the size of the reduced mesh given in [\(3.12\)](#). A justification for our claim is as follows.

The key difference between a SAM and a Cartesian mesh is in the cost of the `get_location_id` routine. Recall that the routine `get_location_id` (as given in [Algorithm 3.2](#)) finds the id of the mesh element that contains a given space point. On a SAM—first performing a search on the auxiliary Cartesian mesh that requires $\mathcal{O}(1)$ operations—we require an additional $\mathcal{O}(N_{uc})$ operations to search in the N_{uc} unstructured cells contained inside a single Cartesian mesh element. Thus, as opposed to $\mathcal{O}(1)$ operations on a Cartesian mesh, `get_location_id` routine on a SAM requires $\mathcal{O}(N_{uc})$ operations.

On an unstructured grid, we consider an orthogonal projection operator Π —refer back to [Remark 1](#) for details. To compute the projection, we consider a numerical quadrature with N_{quad} quadrature points inside every cell. To find the shifted location of each of these quadrature points, we require $\mathcal{O}(N_{uc}N_{quad})$ operations. To perform this computation for n number of mesh elements, we need $\mathcal{O}(N_{uc}N_{quad}n)$ operations.

Using the same reasoning as above, one can conclude that, for some $v \in \mathbb{R}^N$, computing the operator $\mathcal{F}(v)$ on a reduced mesh of size n requires $\mathcal{O}(N_{uc}n)$ operations— $\mathcal{O}(N_{uc})$ operations provide the neighbour of a single mesh element. Likewise, adapting a reduced mesh with n elements requires $\mathcal{O}(N_{uc}n)$ operations. Furthermore, the cost of solving the least-squares problem with the `lsqminnorm` routine requires $\mathcal{O}(n)$.

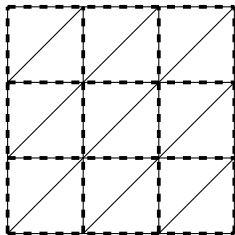


Fig. 5: A sample SAM. Dashed lines—auxiliary Cartesian mesh. Solid lines—unstructured mesh.

6 Numerical Experiments We consider the following test cases. The goal of our numerical experiments is to study the accuracy of the online adaptive reduced mesh technique and compare it to the non-adaptive technique and the FOM.

- (i) **Test-1 (1D Linear advection)** We consider a linear one-dimensional ad-

vection equation with a parameterised advection speed

$$(6.1) \quad \partial_t u(x, t, \mu) + \mu \partial_x u(x, t, \mu) = 0, \quad \forall (x, t, \mu) \in \Omega \times D \times \mathcal{P}.$$

We choose $\Omega = [0, 3]$, $\mathcal{P} = [1, 3]$, and $D = [0, 0.5]$. The initial data reads

$$(6.2) \quad u_0(x, \mu) = \begin{cases} \mu, & x \in [0.5, 1] \\ 0, & \text{else} \end{cases}, \quad \forall \mu \in \mathcal{P}.$$

- (ii) **Test-2 (A moving box function)** We construct a reduced approximation to the set $\{u_N(\cdot, z) : z \in \mathcal{Z}\}$, where $u_N(\cdot, z)$ is a FV approximation to a function $u(\cdot, z)$ that shifts in Ω and changes its "shape" with the parameter. For all $(t, \mu) \in D \times \mathcal{P}$, the function $u(\cdot, z)$ is given as

$$(6.3) \quad u(\cdot, t, \mu) = \begin{cases} \exp(-\mu t), & |x_1 - (\mu + t)| \leq 0.3, |x_2 - t| \leq 0.3 \\ 0, & \text{else} \end{cases}.$$

We choose $D, \mathcal{P} = [0, 1]$, and $\Omega = [-0.5, 2.5]^2$. Note that increasing μ shifts $u(\cdot, t, \mu)$ along the x_1 -direction, and increasing t shifts $u(\cdot, t, \mu)$ along the vector $(t, t)^T$. To compute the FV approximation $u_N(\cdot, z)$, we project $u(\cdot, z)$ onto the FV approximation space. The details related to the projection and the reduced approximation are discussed later.

- (iii) **Test-3 (2D Collisionless radiative transport)** We consider the 2D collisionless radiative transport equation given as [8]

$$(6.4) \quad \begin{aligned} \partial_t u(x, t, \mu) + \cos(\mu) \partial_{x_1} u(x, t, \mu) \\ + \sin(\mu) \partial_{x_2} u(x, t, \mu) = 0, \quad \forall (x, t, \mu) \in \Omega \times D \times \mathcal{P}. \end{aligned}$$

The initial data reads

$$(6.5) \quad u_0(x, \mu) = \begin{cases} 1, & \|x\|_2 \leq 0.2 \\ 0, & \text{else} \end{cases}, \quad \forall \mu \in \mathcal{P}.$$

We set $\Omega = [-1, 1]^2$, $\mathcal{P} = [0, 2\pi]$, and $D = [0, 0.5]$.

6.1 Comparison of the different ROMs In Table 1, we abbreviate the different ROMs that we compare via numerical experiments. For a $z \in \mathcal{I}^{\mathcal{Z}}$, for the S-ROM, we approximate $u_N(\cdot, z)$ in the space $\tilde{\mathcal{X}}_m$ given as

$$(6.6) \quad \tilde{\mathcal{X}}_m := \text{span}\{u_N(\cdot, z_*^{(i)})\}_{i=1, \dots, 4},$$

where $\{z_*^{(i)}\}_i$ are the parameter samples given in Definition 3.1. Thus, $\tilde{\mathcal{X}}_m$ is the same as $\mathcal{X}_m(z)$ but without the spatial transforms. To compute a solution in $\tilde{\mathcal{X}}_m$, we use the residual minimization technique from Subsection 3.4. We are only interested in the accuracy of the S-ROM and do not equip it with any hyper-reduction technique.

REMARK 6 (Accuracy of the S-ROM). *The approximation space $\tilde{\mathcal{X}}_m$ satisfies*

$$\tilde{\mathcal{X}}_m \subseteq \underline{\text{span}\{u_N(\cdot, z^{(i)})\}_{i=1, \dots, N_\mu \times N_t}},$$

where the underlined space is a span of all snapshots and is a standard linear reduced basis space for the solution set $\{u_N(\cdot, z) : z \in \mathcal{Z}\}$. Since the Kolmogorov m -width of this solution set (usually) decays slowly, for a sufficiently small N_μ and N_t , we expect an approximation in the underlined space—and because of the above inclusion, also in $\tilde{\mathcal{X}}_m$ —to be inaccurate. Numerical experiments will corroborate our claim.

Abbreviation	Approximation space	Hyper-reduction
Adp-SS-ROM	$\mathcal{X}_m(z)$	online-adaptive (see Subsection 4.2)
N-Adp-SS-ROM	$\mathcal{X}_m(z)$	non-adaptive (see Subsection 4.1)
SS-ROM	$\mathcal{X}_m(z)$	none
S-ROM	$\tilde{\mathcal{X}}_m$	none

Table 1: *Abbreviations for the different ROMs compared via numerical experiments. See (3.4) and (6.6) for a definition of $\mathcal{X}_m(z)$ and $\tilde{\mathcal{X}}_m$, respectively. The abbreviations SS and S stand for shifted snapshot and snapshot, respectively.*

6.2 Error quantification Recall that N_μ and N_t represent the number of parameter samples along the domains \mathcal{P} and D , respectively—see [Subsection 3.3](#) for details. We quantify the error in our ROM via the relative error

$$(6.7) \quad E(N_t, N_\mu) := \|e\|_{L^\infty(\mathcal{Z})} \quad \text{where} \quad e(z) := \frac{\|u_N(\cdot, z) - u_m(\cdot, z)\|_{L^2(\Omega)}}{\|u_N(\cdot, z)\|_{L^2(\Omega)}}.$$

The reduced solution u_m can result from either of the ROMs listed in [Table 1](#). We approximate the $L^\infty(\mathcal{Z})$ norm via

$$(6.8) \quad \|e\|_{L^\infty(\mathcal{Z})} \approx \max_{z \in \mathcal{Z}_{target}} |e(z)|,$$

where $\mathcal{Z}_{target} \subset \mathcal{Z}$ is a sufficiently dense, problem dependent and finite set of target parameters given later.

REMARK 7 (Software and hardware details). *All the simulations are run using `matlab`, in serial, and on a computer with two Intel Xeon Silver 4110 processors, 16 cores each and 92GB of RAM.*

6.3 Test-1 We choose a constant time-step of $\Delta t = 1/N_x$, which satisfies the CFL-condition (2.4). We choose $N_\mu, N_t = 2$ and $N_x = 10^3$. Furthermore, as a set of target parameters, we choose $\mathcal{Z}_{target} = \{(t_i, \tilde{\mu}_j)\}_{i,j}$, where t_j are the time-instances at which we compute the ROM, and $\{\tilde{\mu}_j\}_j$ are 40 different parameter samples uniformly placed samples inside \mathcal{P} . For the offline phase of the hyper-reduction, we consider five uniformly placed samples inside \mathcal{P} i.e., $m_{hyp} = 5$ in (4.1).

6.3.1 Error comparison For the different ROMs outlined in [Table 1](#), [Table 2](#) compares the error $E(N_\mu, N_t)$. The size of the reduced mesh is $n = N_x \times 5 \times 10^{-3}$, which is 0.5% of the total mesh size. A few observations are in order. Firstly, with a relative error of 1.07, the S-ROM performs poorly. It results in an error that is almost five and ten times larger than that resulting from the Adp-SS-ROM and the SS-ROM, respectively. Secondly, the error resulting from the Adp-SS-ROM is twice of that resulting from the SS-ROM. Given the speed-up offered by the Adp-SS-ROM (see the results below), we insist that this loss in accuracy is reasonable. Lastly, the N-Adp-SS-ROM showed large oscillations and appeared to be unstable, which resulted in extremely large error values. Increasing the size of the reduced mesh (as discussed next) makes N-Adp-SS-ROM stable and provides acceptable accuracy.

The precise reason behind the instability of the N-Adp-SS-ROM is unclear, as yet. Intuitively, we expect that as the residual "moves" along the spatial domain, a fixed reduced mesh is unable to capture the "significant" part of the residual, resulting in instabilities. To further elaborate on this point, for $n = 5$, in [Figure 6](#) we plot

two snapshots of the residual and the cell centres of the reduced mesh. Similar to [Example 4.1](#), for the residual at $z = (0.5, 1.5)$, none of the reduced mesh elements lie inside the support of the residual. In contrast, the adaptive approach accurately tracks the "movement" of the residual and appropriately places the reduced mesh.

	N-Adp-SS-ROM	Adp-SS-ROM	SS-ROM	S-ROM
$E(N_\mu, N_t)$	1.95×10^{30}	0.22	0.11	1.07

Table 2: Results for test case-1. Error comparison between the different ROMs listed in [Table 1](#). Computations performed with $N_\mu, N_t = 2$, $N_x = 10^3$, and $n = N_x \times 5 \times 10^{-3}$. The N-Adp-SS-ROM showed large oscillations and appeared to be unstable, hence the extremely large error values.

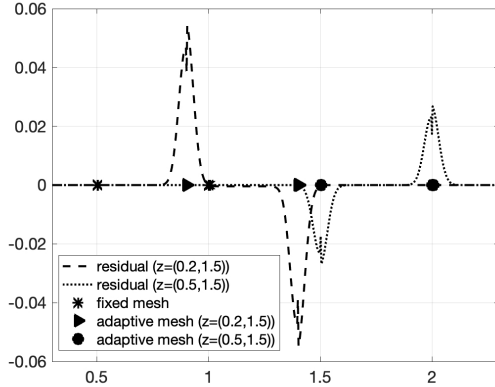


Fig. 6: Results for test case-1. Snapshots of the residual and the centres of the reduced mesh. The size of the reduced mesh is $n = 5$.

6.3.2 $E(N_\mu, N_t)$ versus n For the different sizes of the reduced mesh, we compare the error $E(N_\mu, N_t)$ resulting from the Adp-SS-ROM and the N-Adp-SS-ROM. We consider five different values of the reduced mesh size, $n \in \{100, 200, 400, 800\}$. These values correspond to 10%, 20%, 40% and 80% of the mesh size, respectively. Note that, as the previous study demonstrates, already for $n \ll 100$, the Adp-SS-ROM provides acceptable results. However, for all $n \leq 400$, the N-Adp-SS-ROM showed instabilities, which is the reason behind considering only large values of n .

[Table 3](#) compares the error values. We make the following observations. (i) Increasing n reduces the error for both the ROMs, which is desirable. Since the accuracy of our ROM is limited by our choice of N_t and N_μ , and increasing n can only offer so much accuracy, the error from Adp-SS-ROM stagnates after a value of 0.11. (ii) For all $n \leq 400$, the N-Adp-SS-ROM led to strong oscillations and appeared to be unstable, which resulted in extremely large error values. Increasing n to 800 removes these instabilities and provides reasonable error values. (iii) For all the listed values of n , the Adp-SS-ROM remains stable and provides error values close to those reported for the SS-ROM in [Table 2](#). Note that the Adp-SS-ROM resulted in a larger error value in the previous study because the value of n was smaller.

n ($\%N_x$)	$E(N_\mu, N_t)$	
	Adp-SS-ROM	N-Adp-SS-ROM
100 (10)	0.13	<u>5.6×10^{27}</u>
200 (20)	0.11	<u>1.1×10^{26}</u>
400 (40)	0.11	<u>1.01×10^{13}</u>
800 (80)	0.11	0.11

Table 3: Results for test case-1. Error versus the size of the reduced mesh n . For the underlined values, the N-Adp-SS-ROM showed large oscillations and appeared to be unstable, hence the large error values.

6.3.3 Runtime versus the error We consider the average runtime given as

$$(6.9) \quad \mathcal{C} := \sum_{z \in \mathcal{Z}_{\text{target}}} \mathcal{C}_z / (\#\mathcal{Z}_{\text{target}}),$$

where \mathcal{C}_z represents the cpu-time (measured with the `tic-toc` function of `matlab`) required by the online stage of the ROM (or by the FOM) to compute the solution at the parameter z .

Figure 7 plots the runtime \mathcal{C} and the speed-up against the error $E(N_\mu, N_t)$. We make the following observations. (i) Although not monotonically, the error converges with n . The non-monotonic convergence of the error can be an artefact of the point selection algorithm given in Algorithm 4.1. Additional numerical experiments that compare the different point selection algorithms are required to corroborate our claim. (ii) Increasing n increases the runtime. This is consistent with the fact that the cost of the Adp-SS-ROM scales with n . (iii) At worst, for $n = 320$, the Adp-SS-ROM is 1.8 times faster than the SS-ROM, and at best, for $n = 5$, it is five times faster than the SS-ROM. (iv) The problem is one-dimensional therefore, the explicit time-stepping based FOM is already very efficient. As a result, none of the ROMs provide any speed-up. We refer to test case-3 for a 2D problem where, as compared to the FOM, our hyper-reduction technique offers a significant speed-up.

6.4 Test-2 We set $N_t = N_\mu = 3$, and $N_x = 600$. To compute the SS-ROM, we consider the minimization problem

$$(6.10) \quad \alpha(z) = \arg \min_{y \in \mathbb{R}^4} \|A[\mathcal{E}_z](z)y - b[\mathcal{E}_z](z)\|_{l_2}.$$

Here, \mathcal{E}_z and $A[\mathcal{E}_z](z)$ are as defined earlier, and $b[\mathcal{E}_z](z)$ is a sub-vector of the vector $b(z) = U(z)$. To compute $U(z)$, we project $u(\cdot, z)$ onto the FV approximation space. To perform the projection, we consider tensorized 5×5 Gauss-Legendre quadrature points in each mesh element. The reduced approximation is given by $U_m = A(z)\alpha(z)$. Note that for the current test case, computing the FOM is equivalent to projecting the exact solution onto the FV approximation space. To collect snapshots of the residual, in (4.1), we set $m_{\text{hyp}} = 4$. We choose $\mathcal{Z}_{\text{target}}$ as 100×100 uniformly placed and tensorised points inside \mathcal{Z} .

REMARK 8 (No time-stepping). *The above minimization problem does not involve a time-stepping scheme. This allows us to study the errors resulting from the reduced approximation, residual minimization and hyper-reduction without the errors introduced from the time-stepping scheme.*

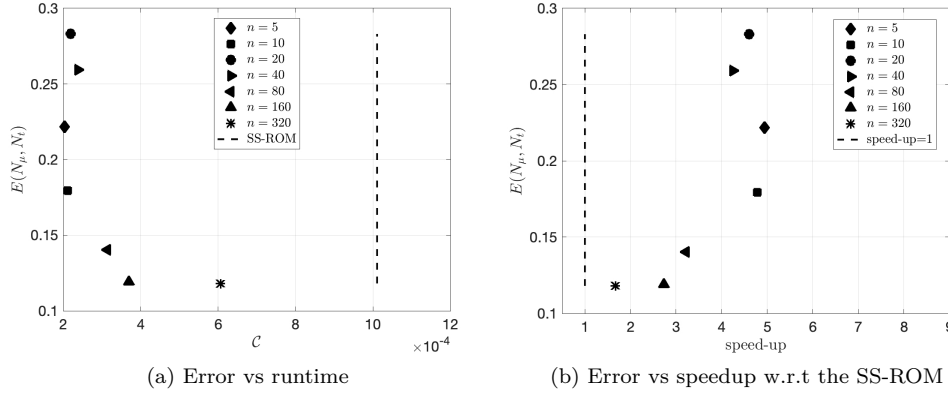


Fig. 7: Results for test case-1 computed with the Adp-SS-ROM. See (6.7) and (6.9) for a definition of the error $E(N_\mu, N_t)$ and the runtime \mathcal{C} , respectively. The dashed line represents (a) the time taken by the SS-ROM, and (b) a speed-up of one.

6.4.1 Error comparison Table 4 presents the error values resulting from the different ROMs listed in Table 1. As the size of the reduced mesh, we choose $n = N_x^2 \times 10^{-2}$, which is 1% of the total mesh size. Both the Adp-SS-ROM and the SS-ROM outperform the S-ROM. The error values resulting from the S-ROM are almost 4.5 times of those resulting from the Adp-SS-ROM. At least for the present test case and our choice of n , our online adaptive hyper-reduction technique introduces almost no error in the SS-ROM.

Unlike the previous test case, the N-Adp-SS-ROM did not exhibit large oscillations, instabilities or extremely large error values. The reason being that the minimization problem in (6.10) does not involve a time-stepping scheme—see Remark 8 above. This prevents error accumulation over time, which, along with a poor placement of the reduced mesh, was one of the reasons why the N-Adp-SS-ROM was unstable in the previous study. For the N-Adp-SS-ROM, there exist target parameters without a single reduced mesh element lying inside the support of the residual. As a result, the solution to the minimization problem (6.10) is zero, leading to a relative error of one.

	N-Adp-SS-ROM	Adp-SS-ROM	SS-ROM	S-ROM
$E(N_\mu, N_t)$	1	0.19	0.18	0.84

Table 4: Results for test case-2. Computations performed with $N_\mu, N_t = 3$, $N_x = 600$, and $n = N_x^2 \times 10^{-2}$. Error comparison between the different ROMs listed in Table 1.

6.4.2 $E(N_\mu, N_t)$ versus n For different values of n , Figure 8 compares the error $E(N_\mu, N_t)$ resulting from the N-Adp-SS-ROM and the Adp-SS-ROM. Our observations remain similar to the previous test case. The N-Adp-SS-ROM requires a large reduced mesh to achieve an acceptable accuracy—at least $n = 5.76 \times 10^4$ reduced mesh elements, which is 16% of the total mesh size, are required to achieve an error of 0.19. In contrast, the Adp-SS-ROM provides similar accuracy with a reduced mesh that is just 0.5% of the total mesh size. As before, our choice of N_μ and N_t limit the

accuracy, resulting in error stagnation.

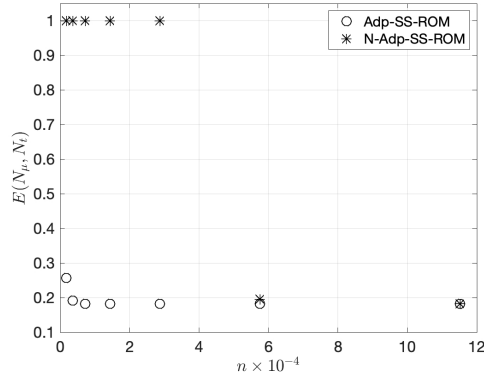


Fig. 8: Results for test case-2. Error versus the size of the reduced mesh n . Computations performed with $N_t = N_x = 3$.

6.4.3 Runtime versus error Consider the average runtime \mathcal{C} defined in (6.9). For the Adp-SS-ROM, Figure 9 plots the runtime and the speed-up against the error. A few observations follow. (i) The error decreases monotonically upon increasing n , which is desirable. (ii) At best, for $n = 1.8 \times 10^3$, the Adp-SS-ROM is 30 times faster and 1.3 times worse in accuracy than the SS-ROM. (iii) At worst, for $n = 115.2 \times 10^3$, the Adp-SS-ROM is almost 8.5 times faster (and similar in accuracy) than the SS-ROM. (iv) Computing the FOM involves projecting a function onto the FV approximation space, which is a cheap operation. Therefore, none of the ROMs offer any speed-up. We refer to the following test case that considers a more realistic scenario and presents the speed-up offered by our hyper-reduction technique.

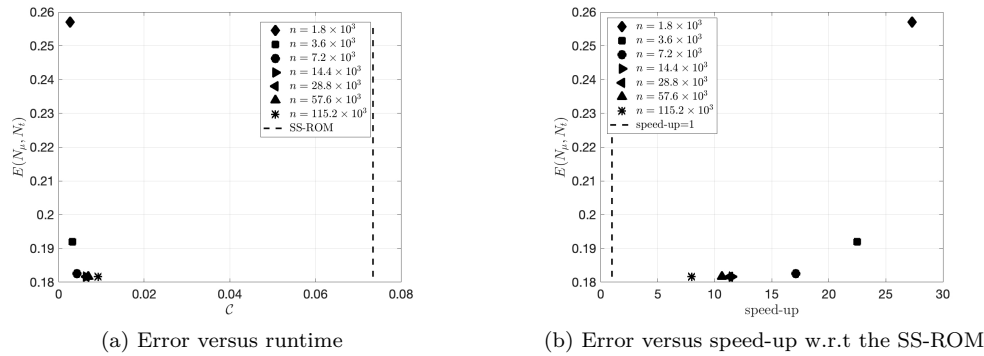


Fig. 9: Results for test case-2, computed with the Adp-SS-ROM. The dashed line represents (a) the time taken by the SS-ROM, and (b) a speed-up of one.

6.5 Test-3 We discretize Ω with a $N_x \times N_x$ Cartesian grid and we choose $N_x = 800$. We use a constant time step of $\Delta t = \Delta x/2$. We set $N_\mu = N_t = 6$.

To collect snapshots of the residual, we take 5 uniformly placed samples from \mathcal{P} i.e., $m_{hyp} = 5$ in (4.1). We study the ROM at the target parameters $\mathcal{Z}_{target} = \{(t_i, \tilde{\mu}_j)\}_{i,j}$. Here, $\{t_j\}_j$ represent the time-instances at which we compute the ROM, and $\{\tilde{\mu}_i\}_i$ are 50 uniformly placed samples inside \mathcal{P} .

6.5.1 Error comparison We choose a reduced mesh that contains 2% of the total mesh elements. Table 5 shows the error $E(N_\mu, N_t)$ for the different ROMs. We make the following observations. (i) Both the Adp-SS-ROM and the SS-ROM outperform the S-ROM. (ii) The maximum error resulting from the Adp-SS-ROM is almost 1.3 times of that resulting from the SS-ROM. Given that Adp-SS-ROM is 50 times more efficient than the SS-ROM—see the discussion below—we insist that the loss in accuracy introduced via hyper-reduction is acceptable. (iii) The N-Adp-SS-ROM shows large oscillations resulting in large error values. Nonetheless, same as earlier, increasing the size of the reduced mesh removes these instabilities and provides an acceptable accuracy.

	N-Adp-SS-ROM	Adp-SS-ROM	SS-ROM	S-ROM
$E(N_\mu, N_t)$	18.75×10^3	0.29	0.21	1.06

Table 5: Results for test case-3. Computations performed with $N_\mu, N_t = 6$, $N_x = 800$, and $n = N_x \times 2 \times 10^{-2}$. Error comparison between the different ROMs listed in Table 1. The N-Adp-SS-ROM showed large oscillations and appeared to be unstable, hence the extremely large error values.

6.5.2 Runtime versus the error For the Adp-SS-ROM, Figure 10 plots the average runtime and the speed-up versus the error $E(N_\mu, N_t)$. We make the following observations. (i) Increasing n increases the runtime and decreases the speed-up, which is as expected. Beyond $n = 25.6 \times 10^3$, as compared to the FOM, the Adp-SS-ROM does not offer any speed-up. (ii) The lowest runtime and the maximum speed-up of 7.8 corresponds to a reduced mesh that contains 0.5% of the total mesh elements. The relative error is 0.32, which is one-third of that resulting from the S-ROM and is 1.5 times of that resulting from the SS-ROM—see Table 5. The accuracy loss as compared to the SS-ROM is acceptable given that the Adp-SS-ROM offers a speed-up of two orders-of-magnitude.

6.5.3 Runtime split We split the runtime \mathcal{C} into four major parts. (i) \mathcal{C}_{adapt} , the average runtime to adapt the reduced mesh, (ii) \mathcal{C}_A , the average runtime to compute the matrix $A(t_{k+1}, \mu)$ given in (3.7) (or $A[\mathcal{E}_{t_{k+1}, \mu}(t_{k+1}, \mu)]$ in the case of hyper-reduction). (iii) \mathcal{C}_b , the average runtime to compute the vector $b(t_k, \mu)$ given in (3.11). (iv) \mathcal{C}_{ls} , the average runtime to solve the least-squares problem in (3.10). For $N_x = 800$ and $n = N_x^2 \times 2 \times 10^{-2}$, Figure 11 compares the different runtime for the Adp-SS-ROM. By far, computing the vector $b(t_k, \mu)$ is the most expensive part of the algorithm—it takes almost 70% of the total runtime. It is noteworthy that the combined cost of solving the least-squares problem and adapting the reduced mesh is less than 10% of the total runtime. Although not shown in the plot, increasing N_x has almost no effect on the runtime.

6.5.4 Visualization of the reduced mesh For $N_x = 500$ and $n = N_x^2 \times 5 \times 10^{-3}$, Figure 12 presents the centres of the reduced mesh computed using the adaptive and the non-adaptive technique. The reduced mesh resulting from the non-adaptive

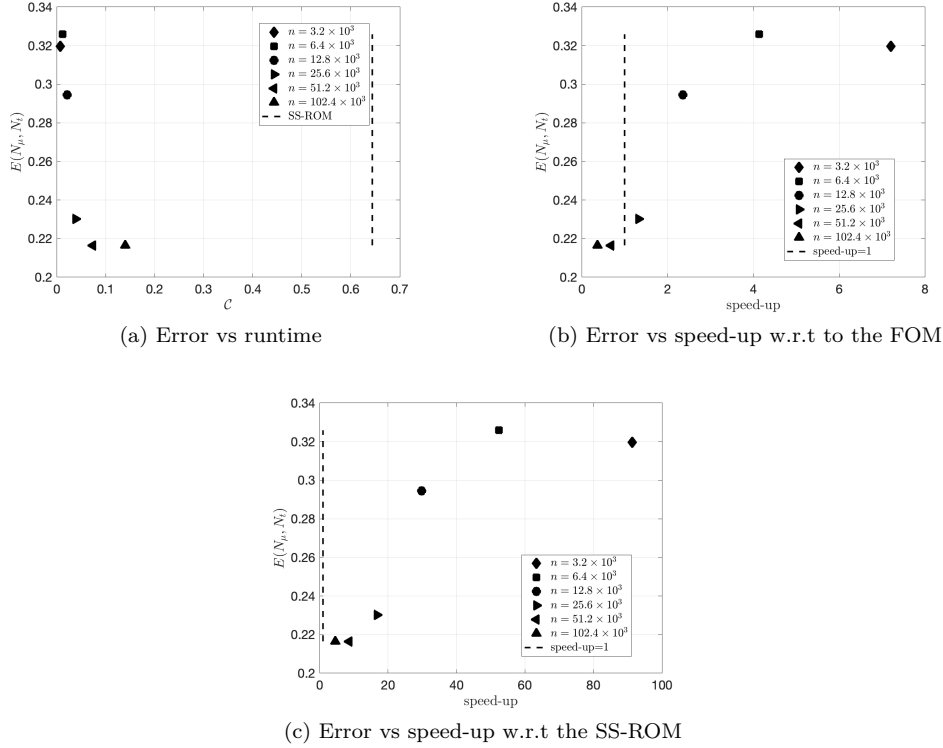


Fig. 10: Results for test case-3, computed with the Adp-SS-ROM. Computations performed with $N_\mu = N_t = 6$, and $N_x = 800$. See (6.7) and (6.9) for a definition of $\mathcal{E}(N_\mu, N_t)$ and \mathcal{C} , respectively. The dotted line indicates (a) the runtime of the SS-ROM, (b) and (c) speed-up of one.

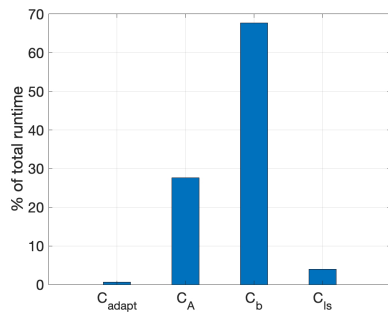


Fig. 11: Results for test case-3. Runtime split for the online-adaptive hyper-reduced ROM. Computations performed with $N_t = N_\mu = 6$.

technique is fixed in the parameter space. Most of its elements are centred around the origin and none lie in the "significant/non-zero" part of the residual. Apparently,

this—as noted earlier—results in an unstable ROM. In contrast, by tracking the “movement” of the residual, the adaptive technique changes the reduced mesh with the parameter and places it where the residual is large/non-zero.

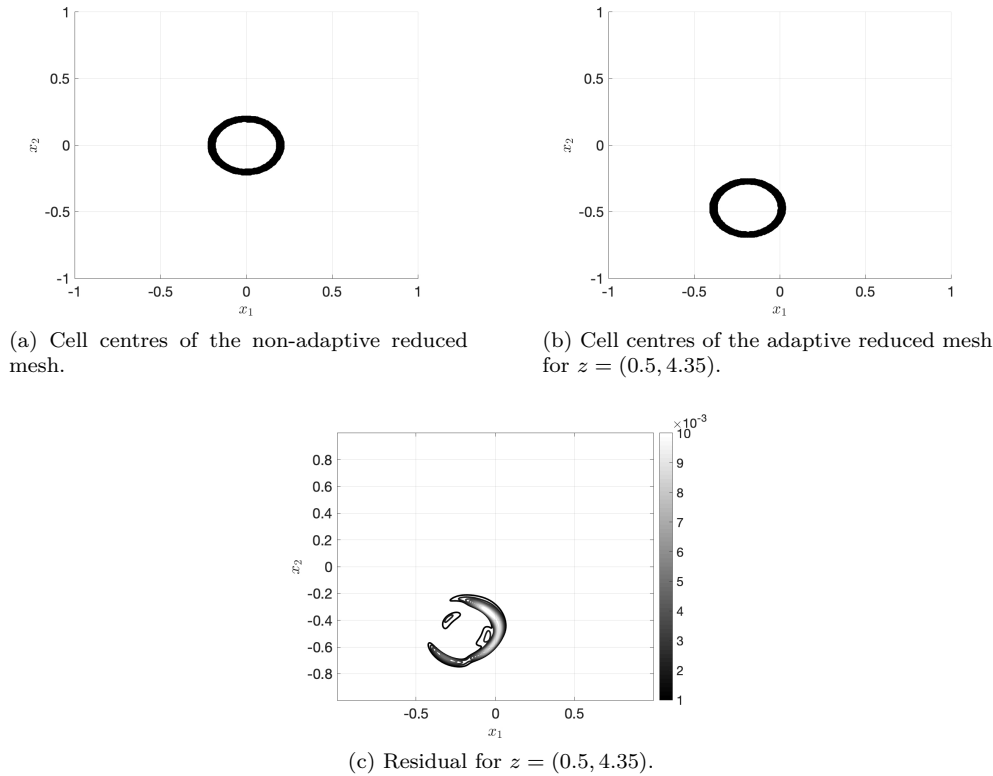


Fig. 12: Results for test case-3. Results computed with $N_\mu = N_t = 6$ and $N_x = 500$.

7 Conclusions We propose an online-adaptive hyper-reduction technique for the nonlinear reduced order modelling of transport dominated problems. Our nonlinear approximation space is a span of shifted snapshots and we seek a solution using residual minimization. Through a cost analysis, we conclude that residual minimization is (at least) as expensive as the full-order model. To reduce the cost of residual minimization, we perform residual minimization over a reduced mesh i.e., over a subset of the full mesh. Using numerical and analytical examples we show that, similar to the solution, the residual exhibits a transport-type behaviour. This makes the use of a fixed parameter-independent reduced mesh both inaccurate and inefficient. To account for the transport-type behaviour of the residual, we introduce online-adaptivity in the reduced mesh.

Empirically, we establish that for the same size of the reduced mesh, the online-adaptive technique greatly outperforms a non-adaptive technique. For a sufficiently small reduced mesh—almost 1% to 2% the size of the full mesh—the adaptive technique provides reasonable accuracy. In contrast, for such small sizes of the reduced mesh, the non-adaptive technique lead to an unstable reduced-order model, resulting

in oscillations and extremely large error values. Nonetheless, at the expense of a high computational cost, increasing the size of the reduced mesh to about 20%-50% of the total mesh size improved the accuracy of the non-adaptive technique.

Appendix A. Example demonstrating the role of φ .

EXAMPLE A.1 (Introducing regularity via φ). Consider the set $\mathcal{G} := \{g(\cdot, z) : \mu \in \mathcal{Z}\} \subset L^2(\mathbb{R})$, where $g(\cdot, z)$ is a step function that scales and shifts to the right, and is given as

$$g(x, z) := \begin{cases} 1 + z, & x \leq z \\ 0, & x > z \end{cases}, \quad z \in \mathcal{Z} := [0, 1].$$

For every $x \in \Omega$, $g(x, \cdot)$ belongs to $H^{1/2}(\mathcal{Z})$, which prohibits its approximability in a linear space. Indeed, one can prove that the Kolmogorov m -width of \mathcal{G} scales as $\mathcal{O}(1/\sqrt{m})$ —see [5] for a proof.

For some $\hat{z} \in \mathcal{Z}$, consider the set \mathcal{G}_φ that consists of all the step functions shifted such that their discontinuities are aligned with the discontinuity in $g(\cdot, \hat{z})$

$$\begin{aligned} \mathcal{G}_\varphi &:= \{g(\varphi(\cdot, z, \hat{z}), \hat{z}) : \varphi(x, z, \hat{z}) = x - (z - \hat{z}), \hat{z} \in \mathcal{Z}\}, \\ &= \{(1 + \hat{z})g(\cdot, z) : \hat{z} \in \mathcal{Z}\}. \end{aligned}$$

We conclude that, for all $x \in \Omega$, the function $g(\varphi(x, \cdot, \hat{z}), \hat{z})$ is smooth. Furthermore, one can conclude that \mathcal{G}_φ is contained in the span of any single function taken from \mathcal{G}_φ . Thus, for $m \geq 1$, its Kolmogorov m -width is zero.

A.1 Snapshots of the shift As mentioned in the introduction, we want $u(\varphi(x, z, \cdot), \cdot)$ to be sufficiently regular. To this end, for all $z^{(i)}, z^{(j)} \in \mathcal{Z}$, one seeks to (at least approximately) satisfy the matching condition

$$(A.1) \quad \varphi(\mathcal{D}(z^{(i)}), z^{(j)}, z^{(i)}) = \mathcal{D}(z^{(i)}),$$

where $\mathcal{D}(z^{(i)}) \subset \Omega$ and $\mathcal{D}(z^{(j)}) \subset \Omega$ represent the point/curve/surface of discontinuity in $u(\cdot, z^{(i)})$ and $u(\cdot, z^{(j)})$, respectively. With our spatial shift ansatz for φ given in (1.4), the matching condition transforms to

$$(A.2) \quad \mathcal{D}(z^{(i)}) = \mathcal{D}(z^{(j)}) + c(z^{(i)}, z^{(j)}).$$

To approximate $\mathcal{D}(z^{(j)})$ (and $\mathcal{D}(z^{(i)})$), we apply to $u_N(\cdot, z^{(i)})$ the multi-resolution-analysis (MRA) based troubled cell indicator proposed in [32]—any other shock-detection technique (for instance, from [13, 24]) also suffices.

In general, the above condition is (very) restrictive. For instance, in a 1D spatial domain, the condition holds only if the solution has a single shock or multiple shocks that move with the same velocity. However, the condition is violated for two shocks moving with different velocities. Furthermore, in a multi-dimensional setting, even a single shock that changes in length violates the above condition.

Despite the restrictions of the above condition, empirically, we observe that a spatial shift provides accurate results for problems that approximately satisfy the above relation. For instance, in a multi-dimensional setting, $\mathcal{D}(z^{(i)})$ might be a translation of $\mathcal{D}(z^{(j)})$ but with an elongation. If the elongation is not significant then, we recover a reasonable snapshot transformation via shifting. Similarly, when $\mathcal{D}(z^{(i)})$ has the same length as $\mathcal{D}(z^{(j)})$ but is both a translation and a rotation of $\mathcal{D}(z^{(j)})$, we expect a spatial shift to provide reasonable results if the rotation is not significant.

For the above reasons, we do not strictly impose the discontinuity matching condition given in (A.2). Rather, we develop upon the L2-minimization technique proposed in [18, 27, 29, 30, 33]. We define the set $\mathcal{B}(z^{(j)}, z^{(i)}) \subset \mathbb{R}^d$ that contains all possible shifts that match the respective points in $\mathcal{D}(z^{(j)})$ and $\mathcal{D}(z^{(i)})$. Equivalently,

$$(A.3) \quad \mathcal{B}(z^{(j)}, z^{(i)}) := \{c^* : c^* = x_i^* - x_j^*, x_i^* \in \mathcal{D}(z^{(i)}), x_j^* \in \mathcal{D}(z^{(j)})\}.$$

Out of all the possible shifts in $\mathcal{B}(z^{(j)}, z^{(i)})$, we select the one that solves the minimization problem

$$(A.4) \quad c(z^{(j)}, z^{(i)}) = \arg \min_{c^* \in \mathcal{B}(z^{(j)}, z^{(i)})} \|u_N(\Theta[c^*], z^{(i)}) - u_N(\cdot, z^{(j)})\|_{L^2(\Omega)}.$$

Above, $\Theta[c^*](x) = x - c^*$ and is as given in (1.4). We solve the above problem via enumeration. In our numerical experiments, the set $\mathcal{B}(z^{(j)}, z^{(i)})$ is not too large and a solution via enumeration is affordable.

Appendix B. Shifting residuals. The definition of the residual given in (3.6) provides

$$(B.1) \quad \begin{aligned} & \mathcal{T}[-c(t_{k+1}, \mu, z_{ref})] \text{Res}(U_m(t_{k+1}, \mu), U_m(t_k, \mu)) \\ &= \mathcal{T}[-c(t_{k+1}, \mu, z_{ref})] (U_m(t_{k+1}, \mu) - (U_m(t_k, \mu) + \Delta t \times \mathcal{F}(U_m(t_k, \mu)))). \end{aligned}$$

We simplify the different terms appearing on the right. Using the matrix-product form of the reduced snapshot $U_m(t_{k+1}, \mu)$, we find

$$(B.2) \quad \begin{aligned} & \mathcal{T}[-c(t_{k+1}, \mu, z_{ref})] U_m(t_{k+1}, \mu) \\ &= \sum_i \alpha_i(t_{k+1}, \mu) \mathcal{T}[-c(t_{k+1}, \mu, z_{ref})] \mathcal{T}[c(t_{k+1}, \mu, z_*^{(i)})] U(z_*^{(i)}) \\ &= \sum_i \alpha_i(t_{k+1}, \mu) \mathcal{T}[c(t_{k+1}, \mu, z_*^{(i)}) - c(t_{k+1}, \mu, z_{ref})] U(z_*^{(i)}) \\ &= \sum_i \alpha_i(t_{k+1}, \mu) \mathcal{T}[c(z_{ref}, t_{k+1}, \mu) + c(t_{k+1}, \mu, z_*^{(i)})] U(z_*^{(i)}) \\ &= \sum_i \alpha_i(t_{k+1}, \mu) \mathcal{T}[c(z_{ref}, z_*^{(i)})] U(z_*^{(i)}). \end{aligned}$$

The third and the fourth equalities are a result of (C1) and (C2), respectively. Using the assumed L^∞ stability of the ROM, we find

$$(B.3) \quad \mathcal{T}[-c(t_{k+1}, \mu, z_{ref})] U_m(t_k, \mu) = \sum_i \alpha_i(t_k, \mu) \mathcal{T}[c(z_{ref}, z_*^{(i)})] U(z_*^{(i)}) + \mathcal{O}(1).$$

The commutation property (C3) simplifies the \mathcal{F} term and provides

$$(B.4) \quad \begin{aligned} & \Delta t \times \mathcal{T}[-c(t_{k+1}, \mu, z_{ref})] \mathcal{F}(U_m(t_k, \mu)) \\ &= \Delta t \times \mathcal{F} \left(\sum_i \alpha_i(t_k, \mu) \mathcal{T}[c(z_{ref}, z_*^{(i)})] U(z_*^{(i)}) + \mathcal{O}(1) \right). \end{aligned}$$

Since $\mathcal{F} \in W^{1,\infty}(\mathbb{R}^N)$, we find the desired result.

References.

- [1] Abgrall, R., Amsallem, D., and Crisovan, R. (2016). Robust model reduction by L1-norm minimization and approximation via dictionaries: application to nonlinear hyperbolic problems. *Advanced Modeling and Simulation in Engineering Sciences*, 3(1):1.
- [2] Astrid, P. (2004). Fast reduced order modeling technique for large scale LTV systems. In *Proceedings of the 2004 American Control Conference*, volume 1, pages 762–767.
- [3] Astrid, P., Weiland, S., Willcox, K., and Backx, T. (2008). Missing point estimation in models described by proper orthogonal decomposition. *IEEE Transactions on Automatic Control*, 53(10):2237–2251.
- [4] Benner, P., Gugercin, S., and Willcox, K. (2015). A survey of projection-based model reduction methods for parametric dynamical systems. *SIAM Review*, 57(4):483–531.
- [5] Benner, P., Ohlberger, M., Cohen, A., and Willcox, K. (2017). *Model Reduction and Approximation*. Society for Industrial and Applied Mathematics, Philadelphia, PA.
- [6] Cagniard, N., Maday, Y., and Stamm, B. (2019). Model order reduction for problems with large convection effects. In *Contributions to Partial Differential Equations and Applications*, pages 131–150. Springer International Publishing, Cham.
- [7] Carlberg, K., Farhat, C., Cortial, J., and Amsallem, D. (2013). The GNAT method for non-linear model reduction: Effective implementation and application to computational fluid dynamics and turbulent flows. *Journal of Computational Physics*, 242:623 – 647.
- [8] Cercignani, C. (1988). *The Boltzmann Equation and Its Applications*. Springer, 67 edition.
- [9] Dahmen, W., Plesken, C., and Welper, G. (2014). Double greedy algorithms: Reduced basis methods for transport dominated problems. *ESAIM: M2AN*, 48(3):623–663.
- [10] Ehrlacher, V., Lombardi, D., Mula, O., and Vialard, F.-X. (2019). Nonlinear model reduction on metric spaces. Application to one-dimensional conservative PDEs in Wasserstein spaces. *ESAIM: Mathematical Modelling and Numerical Analysis*.
- [11] Eymard, R., Gallouët, T., and Herbin, R. (2000). Finite volume methods. *Handbook of numerical analysis*, 7:713–1018.
- [12] Gerbeau, J. F. and Lombardi, D. (2014). Approximated Lax pairs for the reduced order integration of nonlinear evolution equations. *Journal of Computational Physics*, 265:246 – 269.
- [13] Krivodonova, L., Xin, J., Remacle, J.-F., Chevaugeon, N., and Flaherty, J. (2004). Shock detection and limiting with discontinuous Galerkin methods for hyperbolic conservation laws. *Applied Numerical Mathematics*, 48(3):323 – 338.
- [14] Lee, K. and Carlberg, K. T. (2020). Model reduction of dynamical systems on nonlinear manifolds using deep convolutional autoencoders. *Journal of Computational Physics*, 404:108973.
- [15] LeVeque, R. J. (2002). *Finite Volume Methods for Hyperbolic Problems*. Cambridge Texts in Applied Mathematics. Cambridge University Press.
- [16] Mojgani, R. and Balajewicz, M. (2020). Physics-aware registration based auto-encoder for convection dominated PDEs. *arXiv:2006.15655*.
- [17] Mowlavi, S. and Sapsis, T. P. (2018). Model order reduction for stochastic dynamical systems with continuous symmetries. *SIAM Journal on Scientific Computing*,

- 40(3):A1669–A1695.
- [18] Nair, N. J. and Balajewicz, M. (2019). Transported snapshot model order reduction approach for parametric, steady-state fluid flows containing parameter-dependent shocks. *International Journal for Numerical Methods in Engineering*, 117(12):1234–1262.
 - [19] Ohlberger, M. and Rave, S. (2013). Nonlinear reduced basis approximation of parameterized evolution equations via the method of freezing. *Comptes Rendus Mathematique*, 351(23):901 – 906.
 - [20] Peherstorfer, B. (2018). Model reduction for transport-dominated problems via online adaptive bases and adaptive sampling. *arXiv:1812.02094*.
 - [21] Pissanetzky, S. and Basombrío, F. G. (1981). Efficient calculation of numerical values of a polyhedral function. *International Journal for Numerical Methods in Engineering*, 17(2):231–237.
 - [22] Quarteroni, A., Manzoni, A., and Negri, F. (2016). *Reduced Basis Methods for Partial Differential Equations: An Introduction*. Springer International Publishing.
 - [23] Raissi, M., Perdikaris, P., and Karniadakis, G. (2019). Physics-informed neural networks: A deep learning framework for solving forward and inverse problems involving nonlinear partial differential equations. *Journal of Computational Physics*, 378:686 – 707.
 - [24] Ray, D. and Hesthaven, J. S. (2019). Detecting troubled-cells on two-dimensional unstructured grids using a neural network. *Journal of Computational Physics*, 397:108845.
 - [25] Reiss, J., Schulze, P., Sesterhenn, J., and Mehrmann, V. (2018). The shifted proper orthogonal decomposition: A mode decomposition for multiple transport phenomena. *SIAM Journal on Scientific Computing*, 40(3):A1322–A1344.
 - [26] Rim, D. and Mandli, K. T. (2018). Displacement interpolation using monotone rearrangement. *SIAM/ASA Journal on Uncertainty Quantification*, 6(4):1503–1531.
 - [27] Rim, D., Moe, S., and LeVeque, R. J. (2018). Transport reversal for model reduction of hyperbolic partial differential equations. *SIAM/ASA Journal on Uncertainty Quantification*, 6(1):118–150.
 - [28] Rim, D., Peherstorfer, B., and Mandli, K. T. (2019). Manifold approximations via transported subspaces: Model reduction for transport-dominated problems. *arXiv:1912.13024*.
 - [29] Rowley, C. W. and Marsden, J. E. (2000). Reconstruction equations and the Karhunen–Loève expansion for systems with symmetry. *Physica D: Nonlinear Phenomena*, 142(1):1 – 19.
 - [30] Taddei, T. (2020). A registration method for model order reduction: Data compression and geometry reduction. *SIAM Journal on Scientific Computing*, 42(2):A997–A1027.
 - [31] Taddei, T., Perotto, S., and Quarteroni, A. (2015). Reduced basis techniques for nonlinear conservation laws. *ESAIM: M2AN*, 49(3):787–814.
 - [32] Vuik, M. J. and Ryan, J. K. (2014). Multiwavelet troubled-cell indicator for discontinuity detection of discontinuous Galerkin schemes. *Journal of Computational Physics*, 270:138 – 160.
 - [33] Welper, G. (2017). Interpolation of functions with parameter dependent jumps by transformed snapshots. *SIAM Journal on Scientific Computing*, 39(4):A1225–A1250.
 - [34] Welper, G. (2020). Transformed snapshot interpolation with high resolution transforms. *SIAM Journal on Scientific Computing*, 42(4):A2037–A2061.